SISSA preprint 63/2016/MATE

Non-linear Schrödinger system for the dynamics of a binary condensate: theory and 2D numerics

Alessandro Michelangeli

Institute of Mathematics, Ludwig Maximilian University of Munich,
Theresienstr. 39, 80333 Munich, Germany
and International School for Advanced Studies – SISSA,
via Bonomea 265, 34136 Trieste, Italy

E-mail: michel@math.lmu.de

Giuseppe Pitton

International School for Advanced Studies – SISSA
via Bonomea 265, 34136 Trieste, Italy

E-mail: gpitton@sissa.it

Abstract. We present a comprehensive discussion of the mathematical framework for binary Bose-Einstein condensates and for the rigorous derivation of their effective dynamics, governed by a system of coupled non-linear Gross-Pitaevskii equations. We also develop in the 2D case a systematic numerical study of the Gross-Pitaevskii systems in a wide range of relevant regimes of population ratios and intra-species and inter-species interactions. Our numerical method is based on a Fourier collocation scheme in space combined with a fourth order integrating factor scheme in time.

PACS numbers: 02.30.Jr, 02.60.Cb, 02.70.Hm, 02.70.Jn, 67.85.De, 67.85.Fg

Keywords: Bose-Einstein condensation, multi-component mixtures, one-body reduced density matrix, scaling limits, non-linear Gross-Pitaevskii system, Fourier collocation method; integrating factor method.

1. Introduction

Bose-Einstein condensation (also BEC henceforth) is the intensely investigated quantum phenomenon that occurs in large systems of indistinguishable bosons when a macroscopic number of particles occupies the same one-body state [50]. Within the vast research field that followed the first realisation of BEC in dilute atomic gases [1, 16], our present analysis focuses on the *dynamics of mixtures of condensates*, a fascinating feature shown by BEC on which much interest has been recently drawn to in experiments and theoretical studies.

Binary mixtures of condensates are mixtures of two distinguishable species of bosons, which coexist in the same spatial region and display BEC in each component, and where interactions are present both between particles of the same species and of different species, however with no inter-species transition.

Once the system is prepared in such conditions, it evolves in time with a many-body dynamics that is conceptually simple but enormously complicated to solve, virtually inaccessible. In suitable experimental conditions (that include ultra-low temperature, high dilution, and weak interactions) one observes that the two coexisting condensates preserve their individuality also at later times and it is possible to give an effective dynamics of the system in terms of the much simpler description of the two condensate profiles. This yields a system of *two coupled cubic non-linear Schrödinger equations* (customarily referred to as *Gross-Pitaevskii equations*) that indeed describe the time evolution of each profile in agreement with the experiments. While relevant information is thus extracted from the *many-body* dynamics in terms of two *one-body* equations, the effectiveness of the description results in replacing an actual *linear* dynamics with *non-linear* PDEs. This is completely analogous to what happens with a condensate of particles of a single species: in this case one Gross-Pitaevskii equation provides the effective evolution of the condensate profile.

The non-linear Schrödinger/Gross-Pitaevskii system for a binary condensate, see (27) and (32) below, is the object of this work, which has a two-fold nature, theoretical and numerical. First, we outline the mathematical picture in which a satisfactory formalisation of BEC is given, also in the presence of two or more components. This is the well-established picture of the reduced density matrix of the many-body quantum system: in Section 2 we survey the standard mathematical background for this tool and the definition of single- and multi-component BEC.

What rigorous connection links the actual many-body Schrödinger dynamics with the effective system of coupled Gross-Pitaevskii equations is the object of Section 3. The issue of deriving effective evolution equations from the quantum many-body dynamics is very much topical and developed in the current mathematical research. Here we discuss the derivation scheme in the multi-component case, a stream started only recently, with emphasis on the indicators of fragmented BEC, on the suitable scaling limits to adopt, and on their dependence on the dimensionality.

Next, in Section 4 we outline the main features of the Cauchy problem associated to the non-linear Schrödinger/Gross-Pitaevskii system in two spatial dimensions. Indeed, it is possible to derive the effective dynamics from the actual many-body dynamics in the time interval in which the former is well-posed, and at least a H^1-theory is needed for the current known derivation schemes. Local (in time) well-posedness holds for an ample class of interactions and trapping potentials, but as soon as the interactions are attractive and the initial data are sufficiently large, blow-up phenomena may occur.

We then turn to a systematic numerical analysis of the non-linear Gross-Pitaevskii system (32). For a *single-component* Gross-Pitaevskii equation, a variety of numerical methods have been introduced and exploited over the last decade, the *double-component*

case having received considerably less attention. We review the current knowledge in Section 5, also highlighting that for the so far not so systematically investigated case of *collisions* among components, a *substantially higher resolution* is required than all the previous studies, and hence parallel computation is needed in order to resolve the complicated intra- and inter-component interactions developing during the spatial overlap of the two components. In fact, with our numerical code we implement MPI parallel simulations with no difficulties in reaching spatial resolutions of $2^{14} \times 2^{14}$, as opposite to the $\sim 2^8 \times 2^8$ resolutions of previous studies.

In Section 6 we discuss our numerical method, that consists of a Fourier collocation scheme in space combined with a fourth order integrating factor scheme in time, and we set up our accuracy threshold, showing that our simulations satisfy well our fidelity test. We also discuss the initial data, chosen to be well-localised Gaussian profiles for each component, conveniently shot against each other, or placed on top of each other, with or without a spatial confinement.

We then present our results in Section 7. The virtue of our investigation is to cover, through 29 numerical experiments with high resolution, a wide and systematic range of relevant regimes, which include balanced, mildly unbalanced, and strongly unbalanced population ratios, as well as intra-species and inter-species interactions of both repulsive and attractive type. We also explore various magnitudes of the customary miscibility parameter among components.

Specifically, we investigate single one-shot, head-on collisions (Section 7.1), component-over-component relaxations (Section 7.2), and multiple re-collisions within a harmonic trap (Section 7.3). Some of the emergent behaviours are peculiar and qualitatively novel, among which the 'splash' of the ultra-light component in the collision against a heavy one, the 'squeezing-and-shooting' occurring in the collision with intense inter-species attraction, the 'crater' formation in one component profile due to the presence of the other, and the competing effects, on the condensate relaxation and component separation, between the dispersive properties of the linear problem and the attraction among components. Some of them may well inspire analytical studies or even interesting experiments.

2. Background: multi-component BEC

2.1. BEC and density matrix formalism

The crowding phenomenon that originates BEC has a natural formalisation, that was given first by Penrose and Onsager in the 1950's [46], in terms of single-particle reduced density matrix.

For a general formulation, let

$$\mathfrak{h} \;=\; L^2(\Lambda) \otimes \mathbb{C}^{2s+1} \tag{1}$$

be the Hilbert space for a quantum particle of spin $s \in \frac{1}{2}\mathbb{N}_0$ confined in a domain $\Lambda \subset \mathbb{R}^d$

(possibly $\mathbb{R}^d$ itself) and, correspondingly, let

$$\mathcal{H}_{N,\mathrm{sym}} \;=\; \mathfrak{h}_{\mathrm{sym}}^{\otimes N} \tag{2}$$

(the *symmetric* N-fold tensor product of $\mathfrak{h}$) be the Hilbert space for a (bosonic) system of N such particles. A many-body state of this system is described by a density matrix γ_N, namely a positive trace-class operator on $\mathcal{H}_{N,\mathrm{sym}}$ with unit trace.

Associated to γ_N is the so-called one-body marginal (or one-body or single-particle reduced density matrix)

$$\gamma_N^{(1)} \;=\; \mathrm{Tr}_{N-1}\,\gamma_N\,, \tag{3}$$

where the map $\mathrm{Tr}_{N-1} : \mathcal{B}_1(\mathcal{H}_{N,\mathrm{sym}}) \to \mathcal{B}_1(\mathfrak{h})$ is the *partial trace* from trace class operators acting on $\mathcal{H}_{N,\mathrm{sym}}$ to trace class operators acting on $\mathfrak{h}$. $\mathrm{Tr}_{N-1}\,\gamma_N$ is defined, by duality, by

$$\mathrm{Tr}_{\mathfrak{h}}(A\cdot \mathrm{Tr}_{N-1}\,\gamma_N) \;=\; \mathrm{Tr}_{\mathcal{H}}(A\otimes \mathbb{1}_{N-1})\cdot\gamma_N)) \qquad \forall A\in\mathcal{B}(\mathfrak{h}) \tag{4}$$

(here $\mathcal{B}(\mathfrak{h})$ denotes the bounded linear operators on $\mathfrak{h}$). In terms of an arbitrary orthonormal basis $(\xi_k)_k$ of $\mathcal{H}_{N-1,\mathrm{sym}}$ one then has

$$\langle\varphi,(\mathrm{Tr}_{N-1}\,\gamma_N)\psi\rangle_{\mathfrak{h}} \;=\; \sum_k \langle\varphi\otimes\xi_k,\gamma_N\,\psi\otimes\xi_k\rangle_{\mathcal{H}_N} \qquad \forall\varphi,\psi\in\mathfrak{h}\,, \tag{5}$$

and the l.h.s. of (5) is independent of the choice of the basis.

Thus, $\gamma_N^{(1)}$ is obtained by "tracing out" $N-1$ degrees of freedom from γ_N. For concreteness, a system of N spinless ($s=0$) bosons in the *pure* state $\Psi_N \in L^2_{\mathrm{sym}}(\mathbb{R}^{Nd},\mathrm{d}x_1\cdots\mathrm{d}x_N)$ (here $L^2_{N,\mathrm{sim}}$ denotes the wave-functions that are symmetric under permutation of any two variables) has one-body marginal $\gamma_N^{(1)}$ given by the integral kernel

$$\gamma_N^{(1)}(\mathbf{x},\mathbf{x}') \;=\; \int_{\mathbb{R}^{(N-1)d}} \Psi_N(\mathbf{x},\mathbf{x}_2,\dots,\mathbf{x}_N)\,\overline{\Psi_N(\mathbf{x}',\mathbf{x}_2,\dots,\mathbf{x}_N)}\,\mathrm{d}\mathbf{x}_2\cdots\mathrm{d}\mathbf{x}_N\,. \tag{6}$$

As a non-negative, bounded, and self-adjoint operator on $\mathfrak{h}$, $\gamma_N^{(1)}$ has a complete set of real non-negative eigenvalues that sum up to 1, that is, there is an orthonormal basis $(\varphi_j^{(N)})_{j=0}^\infty$ of $\mathfrak{h}$ consisting of eigenvectors of $\gamma_N^{(1)}$ with eigenvalues $(n_j^{(N)})_{j=0}^\infty$ so that

$$\begin{aligned} \gamma_N^{(1)} \;&=\; \textstyle\sum_{j=0}^\infty n_j^{(N)}\,|\varphi_j^{(N)}\rangle\langle\varphi_j^{(N)}|\,,\\ 1\geqslant n_0^{(N)}\geqslant n_1^{(N)}\geqslant\cdots\geqslant 0\,,\qquad &\textstyle\sum_{j=0}^\infty n_j^{(N)}=1\,. \end{aligned} \tag{7}$$

In turn, being $\gamma_N^{(1)}$ the partial trace of a many-body bosonic state γ_N, each such eigenvalue has the natural interpretation of *occupation number*: indeed, since the one-body observable $\mathcal{O}_j \equiv |\varphi_j^{(N)}\rangle\langle\varphi_j^{(N)}|\otimes\mathbb{1}_{N-1}$ has expectation $n_j^{(N)}$ in the many-body state γ_N (as follows from (4)), then $n_j^{(N)}$ expresses *in the sense of the reduced density matrix*, the fraction of particles of the many-body state γ_N which occupy the one-body state $\varphi_j^{(N)}$. This is not at all a statement on the many-body wave-function, which in general has a far more complicated structure than the product of such single-particles eigenstates, yet it becomes an exact description for the ideal case of a completely factorised many-body state.

Within this formalism, *BEC corresponds to having one occupation number of order 1 and all the others of order* $o(1)$ in the number N of particles. Thus, $n_0^{(N)}\sim 1$, $\varphi_0^{(N)}\sim\varphi_0$

and $\gamma_N^{(1)} \sim |\varphi_0\rangle\langle\varphi_0|$: the state $\varphi_0 \in \mathfrak{h}$ is the one-body orbital occupied by Nn_0 particles and is customarily referred to as the *condensate wave-function*. This definition applies both to interacting and non-interacting systems (for no reference to the Hamiltonian is made), and evidently assumes an underlying thermodynamic limit. For bosons in the ground state of a d-dimensional box Λ_L of size L, whose one-body marginal $\gamma_N^{(1)}$ is given by (6) (now with the integration over Λ_L^{N-1}), $\gamma_N^{(1)}(\mathbf{x}, \mathbf{x}')$ is expected to be translation invariant in the thermodynamic limit, and hence the eigenfunction φ_0 belonging to the largest eigenvalue is expected to approach the constant function $L^{-d/2}$: in this case, BEC in the ground state means $L^{-d} \iint_{\Lambda_L \times \Lambda_L} \gamma_N^{(1)}(\mathbf{x}, \mathbf{x}') \mathrm{d}\mathbf{x}\, \mathrm{d}\mathbf{x}' \geqslant c > 0$ as $N \to \infty$, $L \to \infty$, with N/L^d fixed. The latter is the celebrated *off-diagonal long range order* for $\gamma_N^{(1)}$ and provides another customary characterisation of BEC. In Fourier transform it yields the characteristic $\mathbf{k} = \mathbf{0}$ delta-peak of BEC in the momentum distribution.

Remarkably, whereas this is precisely the formalism that encodes the experimental evidence of BEC, for *no* many-body Hamiltonians with genuine interactions has BEC been proved so far, with the only exception of hard core bosons on a lattice at half filling [17, 23]. This leaves a major problem open, in view of which many rigorous results have been obtained within simplified *scaling limits*, i.e., caricatures of the thermodynamic limit as $N \to \infty$ which nevertheless retain an amount of physical features of the actual N-body model [35]. In fact, the whole mathematics of the Bose gas and its condensation is today an extraordinarily rich and active subject [30, 53, 54, 8].

2.2. Depletion and condensate. Complete BEC. Simple BEC.

The admixture of other single-particle configurations into the many-body state that exhibits BEC is called *quantum depletion*: it is quantified, in the above formalism, by the sum of the eigenvalues of all non-macroscopically occupied eigenstates φ_j of $\gamma_N^{(1)}$, say, $\lim_{N\to\infty} \sum_{j\geqslant 1} n_j$ if only for the $j = 0$ level one has $\lim_{N\to\infty} n_0 > 0$. Depletion is theoretically expected to be of the order of the percent for BEC in weakly interacting and dilute Bose gases, as experiments with alkali gases well show [28] (in contrast to liquid helium, with depletion $\sim 90\%$ [46]).

Neglecting depletion as a first approximation, (asymptotically) *complete* BEC on the one-body orbital φ ($\varphi \in \mathfrak{h}$, $\|\varphi\| = 1$) is therefore the emergence, as $N \to \infty$ in the thermodynamic limit, of an eigenvalue 1 of $\gamma_N^{(1)}$ relative to the eigenvector φ, all other eigenvalues tending to zero, that is, $\gamma_N^{(1)}$ converges to the rank-one projection $|\varphi\rangle\langle\varphi|$:

$$\lim_{N\to\infty} \gamma_N^{(1)} \;=\; |\varphi\rangle\langle\varphi| \qquad \text{(complete BEC)}\,. \tag{8}$$

All the a priori inequivalent topologies in which the limit in (8) can be understood (from the trace norm to the weak operator topology) are in fact interchangeable in this specific case, for the convergence of a trace-class operator to a rank-one projection satisfies the bounds (see [36] and [25, Section 2])

$$1 - \langle\varphi, \gamma_N^{(1)}\varphi\rangle \;\leqslant\; \mathrm{Tr}|\,\gamma_N^{(1)} - |\varphi\rangle\langle\varphi|\,| \;\leqslant\; 2\sqrt{1 - \langle\varphi, \gamma_N^{(1)}\varphi\rangle}\,. \tag{9}$$

Condition (8) is naturally interpreted as an almost complete factorisation $\Psi_N \approx \varphi^{\otimes N}$ of the many-body state, but strictly speaking this approximation only holds true in the much weaker form $\gamma_N^{(1)} \approx |\varphi\rangle\langle\varphi|$. (In turn, it can be argued that $\gamma_N^{(1)} \approx |\varphi\rangle\langle\varphi|$ implies a factorisation of the many-body state when an amount $k = o(N)$ of particles are considered, see [36] and [25, Section 2].)

In the more realistic presence of depletion, the notion of complete BEC is naturally replaced by that of *simple* BEC, namely the presence of only one macroscopic occupation number and hence only one non-vanishing eigenvalue of $\gamma_N^{(1)}$ in the thermodynamic limit $N \to \infty$:

$$\begin{aligned} \lim_{N\to\infty} n_0^{(N)} &= n_0 \in (0,1] \\ \lim_{N\to\infty} n_j^{(N)} &= 0 \quad \forall j \geqslant 1 \qquad\qquad \text{(simple BEC)}\,. \\ \text{depletion} &= 1 - n_0 \end{aligned} \tag{10}$$

In practice, this is the case when there is a one-body orbital φ ($\varphi \in \mathfrak{h}$, $\|\varphi\| = 1$) such that all eigenvalues of the difference $\gamma_N^{(1)} - |\varphi\rangle\langle\varphi|$ vanish as $N \to \infty$ (without the difference necessarily vanishes or converges, although in concrete cases one expects $0 < \lim_{N\to\infty} \mathrm{Tr}|\,\gamma_N^{(1)} - |\varphi\rangle\langle\varphi|\,| \ll 1$).

For complete (or simple) BEC on φ, the condensate profile $\gamma_N^{(1)}(x,x)$ is with good approximation described by $|\varphi(x)|^2$.

2.3. Multi-component BEC

In a wide range of current experiments in cold atoms [41, 33, 19], heteronuclear mixtures of two or more different species of bosons are manipulated, namely gases with two or more components each of which is an assembly of identical bosons of a certain species, where a macroscopic occupation of some one-body state is induced in each population.

In the resulting multi-component BEC, particles of different species remain distinguishable and subject to intra-species as well as to inter-species interactions, however with no transition among species. Conceptually such *mixtures of condensates* are equivalent to other recent experimental realisations of great relevance: *double-well condensates*, namely scalar bosons confined in a trap with very deep wells and hence negligible tunnelling, with condensation induced in the population of each well; and *pseudo-spinor condensates*, that consist of a gas of bosons with spin and two macroscopically occupied and virtually uncoupled hyperfine states. The latter is typically the case of ^{87}Rb, owing to its unusually low hyperfine-changing collision rate: spin-changing collisions rather lead to condensate loss and hence depletion increase, instead of interconversion between the two species.

A two-component mixture of condensates is customarily referred to also as *binary condensate*. Binary condensates in dilute alkali gases were observed shortly after the first realisations of Bose-Einstein condensation in 1995: they can be created by sympathetic cooling in a magnetic trap, both in the form of coexisting condensates of atoms, typically ^{87}Rb [42, 20], in two different hyperfine spin levels, or in the form of heteronuclear mixtures such as ^{41}K–^{87}Rb [39], ^{41}K–^{85}Rb [40], ^{39}K–^{85}Rb [34], ^{85}K–^{87}Rb [45].

The mathematical formalism for binary condensate is naturally that of a tensor product of Hilbert spaces, one for each component, in each of which the one-body reduced density matrix is considered: we shall discuss this setting in Section 3.1 below. Despite its striking experimental evidence, no rigorous proof of double-component BEC is known for realistic models of Bose gases. They also motivate an additional theoretical interest concerning their robustness along the many-body Schrödinger evolution, with each component preserving its individuality.

3. Effective dynamics of a two-component mixture of condensates

3.1. The model

We consider a d-dimensional two-component interacting Bose gas consisting of a mixture of two distinct species of N_1 identical bosons of one kind and N_2 identical bosons of the other kind. Inter-species and intra-species two-body spatial interactions are present and no intra-species transition is induced.

The natural Hilbert space for the system is therefore

$$\begin{aligned} \mathcal{H}_{N_1,N_2,\mathrm{sym}} &:= \mathcal{H}_{N_1,\mathrm{sym}} \otimes \mathcal{H}_{N_2,\mathrm{sym}} \\ &= L^2_{\mathrm{sym}}(\mathbb{R}^{N_1 d}, \mathrm{d}\mathbf{x}_1 \cdots \mathrm{d}\mathbf{x}_{N_1}) \otimes L^2_{\mathrm{sym}}(\mathbb{R}^{N_2 d}, \mathrm{d}\mathbf{y}_1 \cdots \mathrm{d}\mathbf{y}_{N_2}) \,, \end{aligned} \tag{11}$$

where $\mathcal{H}_{N,\mathrm{sym}}$ is the N-body bosonic Hilbert space introduced in (2) built upon the one-body Hilbert space $\mathfrak{h} = L^2(\mathbb{R}^d)$. Thus, $\mathcal{H}_{N_1,N_2,\mathrm{sym}}$ consists of square-integrable functions Ψ with two distinguishable sets of d-dimensional variables and

$$\Psi(\mathbf{x}_1, \dots, \mathbf{x}_{N_1}; \mathbf{y}_1, \dots, \mathbf{y}_{N_2})$$

is invariant under exchange of any two x-variables or any two y-variables, with no overall permutation symmetry among the two sets of variables. (General non-pure states, namely density matrices acting on $\mathcal{H}_{N_1,N_2,\mathrm{sym}}$, inherit the same double bosonic symmetry.) The first (resp., second) set of variables, and hence the L^2-space in the first (the second) factor of (11), account for the spatial distribution of particles of the first (second) species, say, species A and B.

The Hamiltonian of the system, as an operator acting on $\mathcal{H}_{N_1,N_2}$, has the form

$$\begin{aligned} H_{N_1,N_2} \;=\; & \sum_{i=1}^{N_1} \Big(-\frac{\hbar^2}{2m_A} \Delta_{\mathbf{x}_i} + U(\mathbf{x}_i) \Big)^{(A)} + \sum_{i<j}^{N_1} V^{(A)}(\mathbf{x}_i - \mathbf{x}_j) \\ & + \sum_{r=1}^{N_2} \Big(-\frac{\hbar^2}{2m_B} \Delta_{\mathbf{y}_r} + U(\mathbf{y}_r) \Big)^{(B)} + \sum_{r<s}^{N_2} V^{(B)}(\mathbf{y}_r - \mathbf{y}_s) \\ & + \sum_{i=1}^{N_1} \sum_{r=1}^{N_2} V^{(AB)}(\mathbf{x}_i - \mathbf{y}_r) \,. \end{aligned} \tag{12}$$

In (12) and in the following the notation is self-explanatory: $T^{(A)}$ is the shortcut for the operator $T \otimes \mathbb{1}_{N_2}$ that acts trivially on the B-factor of $\mathcal{H}_{N_1,N_2,\mathrm{sym}}$ and acts as the operator T on the A-factor, and similarly for $T^{(B)}$; $V^{(A)}$ (resp., $V^{(B)}$) is the potential of the two-body interaction between particles of A-type (resp., of B-type), whereas $V^{(AB)}$ is

the interaction potential between particles of different species; U is a one-body potential that models the confinement of the gas in a trap; m_A and m_B are the masses of the two kinds of particles, and $\hbar$ is Planck's constant.

One can modify (12) (and the discussion that will follow) to more general settings in which particles of different species experience a different confinement, thus introducing two potentials $U_A \neq U_B$, or in which the one-body Hamiltonian $h = -\Delta + U$ (in suitable units) is replaced with a magnetic Schrödinger operator $h = -(\nabla - \mathrm{i}A)^2 + U$ or a semi-relativistic Schrödinger operator $h = \sqrt{1-\Delta} + U$, or with time-dependent trapping potentials $U(x;t)$, etc.

As long as $V^{(AB)} \equiv 0$ in the Hamiltonian, the two components are decoupled and the system consists of two Bose gases with no inter-species interaction: the global many-body state is always factorised into the product of an A-factor and a B-factor and the possible occurrence of condensation in each component is monitored separately in terms of the one-body reduced density matrix constructed with respect to each factor space. In the presence of a non-zero $V^{(AB)}$, the generic state of the system (including the ground state) is not factorised: in particular, an initially factorised state loses its product structure, since the inter-species interaction establishes correlations.

Under standard (and physically realistic) conditions on the various potentials, the Hamiltonian H_{N_1,N_2} is self-adjoint on $\mathcal{H}_{N_1,N_2,\mathrm{sym}}$, thus making the model well-posed. Clearly the action of H_{N_1,N_2} remains in $\mathcal{H}_{N_1,N_2,\mathrm{sym}}$, because H_{N_1,N_2} is symmetric under permutation separately in each set of variables. Therefore, the time evolution $e^{-\mathrm{i}\,t/\hbar H_{N_1,N_2}} \gamma_{N_1,N_2} e^{\mathrm{i}\,t/\hbar H_{N_1,N_2}}$ of a two-component bosonic many-body state (density matrix) γ_{N_1,N_2} along the dynamics generated by H_{N_1,N_2} remains a density matrix on $\mathcal{H}_{N_1,N_2,\mathrm{sym}}$. The number of particles of each kind stays constant in time, with no transfer of particles among the two populations.

3.2. Two-component condensation

Following the remarks of the previous Subsection, the possibility that particles of one species undergo condensation is influenced also by the behaviour of the particles of the other species. The macroscopic occupation of particles of one species into the same one-body state is expressed through an adaptation of the BEC formalism of Section 2.1.

It is natural to exploit the simultaneous partial trace realised by doubling (i.e., tensoring) the map Tr_{N-1} discussed in (3)-(4). This leads to the *"double" reduced density matrix*

$$\gamma^{(1,1)}_{N_1,N_2} \;=\; \mathrm{Tr}_{N_1-1} \otimes \mathrm{Tr}_{N_2-1}\, \gamma_{N_1,N_2} \tag{13}$$

associated with the many-body state (i.e., the density matrix on $\mathcal{H}_{N_1,N_2,\mathrm{sym}}$) γ_{N_1,N_2}. The operation in (13) amounts to tracing out $N_1 - 1$ degrees of freedom of type A and $N_2 - 1$ degrees of freedom of type B from γ_{N_1,N_2}, which results in a density matrix on the Hilbert space $\mathfrak{h} \otimes \mathfrak{h} = L^2(\mathbb{R}^d, \mathrm{d}\mathbf{x}) \otimes L^2(\mathbb{R}^d, \mathrm{d}\mathbf{y})$. For concreteness, a pure state (i.e, a normalised

function) $\Psi_{N_1,N_2} \in \mathcal{H}_{N_1,N_2,\mathrm{sym}}$ has an associated $\gamma^{(1,1)}_{N_1,N_2}$ with integral kernel

$$\begin{aligned}\gamma^{(1,1)}_{N_1,N_2}(\mathbf{x},\mathbf{x}';\mathbf{y},\mathbf{y}') \;&=\; \int_{\mathbb{R}^{d(N_1-1)}}\int_{\mathbb{R}^{d(N_2-1)}} \mathrm{d}\mathbf{x}_2\cdots\mathrm{d}\mathbf{x}_{N_1}\mathrm{d}\mathbf{y}_2\cdots\mathrm{d}\mathbf{y}_{N_2} \\ &\quad\times \Psi_{N_1,N_2}(\mathbf{x},\mathbf{x}_2,\dots,\mathbf{x}_{N_1};\mathbf{y},\mathbf{y}_2,\dots,\mathbf{y}_{N_2}) \\ &\quad\times \overline{\Psi_{N_1,N_2}}(\mathbf{x}',\mathbf{x}_2,\dots,\mathbf{x}_{N_1};\mathbf{y}',\mathbf{y}_2,\dots,\mathbf{y}_{N_2})\,.\end{aligned} \tag{14}$$

By setting $y = y'$ in (14) and performing a further integration in y, one ends up with a density matrix, that we denote with $\gamma^{(1,0)}_{N_1,N_2}$, obtained by tracing out all the B-degrees of freedom and all but one the A-degrees of freedom from the considered many-body state; analogously, $\gamma^{(0,1)}_{N_1,N_2}$ is obtained by setting $x = x'$ in (14) and performing a further integration in x. (In the abstract notation of (13), one writes $\gamma^{(1,0)}_{N_1,N_2} = (\mathrm{Tr}_{N_1-1}\otimes\mathrm{Tr}_{N_2})(\gamma_{N_1,N_2})$ and $\gamma^{(0,1)}_{N_1,N_2} = (\mathrm{Tr}_{N_1}\otimes\mathrm{Tr}_{N_2-1})(\gamma_{N_1,N_2})$.)

By construction, the eigenvalues of $\gamma^{(1,0)}_{N_1,N_2}$ (resp., of $\gamma^{(0,1)}_{N_1,N_2}$) have the natural interpretation of occupation numbers for particles of the species A (resp., B), whence the notion of BEC in one of the two components: complete BEC for particles of the species A (resp., B) occurs when for a normalised $u \in L^2(\mathbb{R}^d,\mathrm{d}x)$ (resp., $v \in L^2(\mathbb{R}^d,\mathrm{d}y)$) in the thermodynamic limit one has $\gamma^{(1,0)}_{N_1,N_2} \to |u\rangle\langle u|$ (resp., $\gamma^{(0,1)}_{N_1,N_2} \to |v\rangle\langle v|$), or also, owing to property (9), $\langle u,\gamma^{(1,0)}_{N_1,N_2}u\rangle \to 1$ (resp., $\langle v,\gamma^{(0,1)}_{N_1,N_2}v\rangle \to 1$).

When both conditions occur, one has *simultaneous* BEC with condensate functions u and v, that is, a two-component condensate. Because of the bounds [37, Lemma 3.1]

$$\begin{aligned}&\max\left\{1-\langle u,\gamma^{(1,0)}_{N_1,N_2}u\rangle\,,\,1-\langle v,\gamma^{(0,1)}_{N_1,N_2}v\rangle\right\} \;\leqslant \\ &\qquad\leqslant\; 1-\langle u\otimes v,\gamma^{(1,1)}_{N_1,N_2}u\otimes v\rangle \\ &\qquad\leqslant\; \left(1-\langle u,\gamma^{(1,0)}_{N_1,N_2}u\rangle\right)+\left(1-\langle v,\gamma^{(0,1)}_{N_1,N_2}v\rangle\right),\end{aligned} \tag{15}$$

two-component complete BEC is equivalent to

$$\lim_{N_1,N_2\to\infty}\gamma^{(1,1)}_{N_1,N_2} \;=\; |u\otimes v\rangle\langle u\otimes v| \;=\; |u\rangle\langle u|\otimes|v\rangle\langle v|\,, \tag{16}$$

namely to the convergence of the double reduced density matrix to the rank-one projection $|u\otimes v\rangle\langle u\otimes v|$ on $\mathfrak{h}\otimes\mathfrak{h}$ in the thermodynamic limit.

Analogously to what remarked after (8), the vanishing of $\gamma^{(1,1)}_{N_1,N_2} - |u\otimes v\rangle\langle u\otimes v|$ is *much weaker* than the vanishing of $\|\Psi_{N_1,N_2} - u^{\otimes N_1}\otimes v^{\otimes N_2}\|$, thus the two-component BEC means $\Psi_{N_1,N_2} \approx u^{\otimes N_1}\otimes v^{\otimes N_2}$ only in the sense of reduced density matrices, i.e., of occupation numbers.

In this formalism, the distinguishability of the two species fixes the ordering in the product $u\otimes v \in \mathfrak{h}\otimes\mathfrak{h}$ of the two condensate functions. Even when $u = v$ is the same function, the double condensation $\gamma^{(1,1)}_{N_1,N_2} \approx |u\otimes u\rangle\langle u\otimes u|$ expresses the fact that each component undergoes BEC with *the same spatial profile* of the condensate: the two condensates then sit on top of each other, while the two species remain distinguishable.

3.3. Scheme for the effective dynamics of the fragmented condensate

The knowledge of the many-body dynamics generated by the Hamiltonian H_{N_1,N_2} requires to solve the Cauchy problem

$$\begin{cases} \mathrm{i}\hbar\,\partial_t \Psi_{N_1,N_2}(t) &= H_{N_1,N_2}\Psi_{N_1,N_2}(t) \\ \Psi_{N_1,N_2}(0) &= \Psi^{(0)}_{N_1,N_2} \end{cases} \tag{17}$$

when the system is prepared and evolves in a pure state

$$\Psi_{N_1,N_2}(t) \;\equiv\; \Psi_{N_1,N_2}(\mathbf{x}_1,\dots,\mathbf{x}_{N_1};\mathbf{y}_1,\dots,\mathbf{y}_{N_2};t)\,,$$

or more generally

$$\begin{cases} \mathrm{i}\hbar\,\partial_t \gamma_{N_1,N_2}(t) &= [H_{N_1,N_2},\gamma_{N_1,N_2}(t)] \\ \gamma_{N_1,N_2}(0) &= \gamma^{(0)}_{N_1,N_2}\,. \end{cases} \tag{18}$$

for a-priori non-pure (mixed) states.

Whereas the existence and uniqueness of a solution to the linear problems (17)-(18) is not an issue, as a well-known consequence of the self-adjointness of the Hamiltonian, and thus the many-body dynamics is well-posed, the explicit determination of the solution is obviously out of reach both analytically and numerically. In fact, the very same initial datum is not accessible exactly, from the experimental point of view.

Moreover, because most observables of interest are one-body or few-body observables, the complete knowledge of the solution $\Psi_{N_1,N_2}(t)$ is redundant: one would only need to determine the behaviour in time of expectations $\langle\Psi_{N_1,N_2}(t),\mathcal{O}_k\Psi_{N_1,N_2}(t)\rangle$ of a k-body observable of interest $\mathcal{O}_k$, with k fixed and small. In particular, for one-particle observables $\mathcal{O}_1$ (for example the one-body position operator in a prescribed region of space), combining (4) and (13) one has

$$\langle\Psi_{N_1,N_2}(t),\mathcal{O}_1\Psi_{N_1,N_2}(t)\rangle \;=\; \mathrm{Tr}_{\mathfrak{h}\otimes\mathfrak{h}}(\gamma^{(1,1)}_{N_1,N_2}(t)\,\mathcal{O}_1)\,, \tag{19}$$

which boils down the problem to studying the time evolution of the double reduced density matrix.

In general, $\gamma^{(1,1)}_{N_1,N_2}(t)$ is no more accessible quantity than $\Psi^{(1,1)}_{N_1,N_2}(t)$: its behaviour in time, induced by the many-body Schrödinger equation, is governed by a complicated hierarchy of equations, one for each marginal of higher order [37, Section 4]. However, in special circumstances of physical relevance the problem becomes much simpler at the reduced density matrix level, significantly in the presence of BEC. In this case, $\gamma^{(1,1)}_{N_1,N_2}\approx|u\otimes v\rangle\langle u\otimes v|$ at time $t=0$, as discussed in (16), and the expected *persistence* of two-component BEC at later times suggests that

$$\gamma^{(1,1)}_{N_1,N_2}(t) \;\approx\; |u(t)\otimes v(t)\rangle\langle u(t)\otimes v(t)| \tag{20}$$

for two functions $u(t)$ and $v(t)$ in $L^2(\mathbb{R}^3)$ which give the profile of the condensate of each species and whose evolution in time is also to be determined. Certainly (20) cannot hold at finite N_1,N_2, due to the amount of correlations established by the interactions $V^{(A)}$, $V^{(B)}$, and $V^{(AB)}$ in (12): it is rather expected in the *thermodynamic limit* $N_1,N_2\to\infty$

under the constraint that each population keeps its relative weight, i.e., imposing that for two constants $c_1, c_2 > 0$, fixed in the experimental preparation, one has

$$\lim_{N_1,N_2\to\infty} \frac{N_j}{N_1+N_2} \;=\; c_j \qquad (j=1,2) \tag{21}$$

(that is, the ratio N_1/N_2 remains asymptotically constant).

The thermodynamic limit is in turn virtually unexplored as far as rigorous results are concerned. As customary, one rather mimics it by suitably rescaling the Hamiltonian with the number of particles, in such a way to retain on the one hand physically relevant features of the real system (such as the energy per particle or the relative ratio between kinetic and interaction energy) and to access on the other hand mathematically exploitable limits $N_1, N_2 \to \infty$.

There is a vast literature on the physical grounds, the mathematical properties, and the applications of suitable scaling limits to many-body models of bosons and fermions, both for stationary (ground state) and dynamical questions [30, 35, 25, 47, 48, 49, 8, 43]. In the present case, being the model already defined on the whole d-dimensional space (i.e., not in a box), the scaling is taken on the potentials, that thus become number-of-particle-dependent:

$$V^{(A)} \;\longrightarrow\; V_N^{(A)}\,, \qquad V^{(B)} \;\longrightarrow\; V_N^{(B)}\,, \qquad V^{(AB)} \;\longrightarrow\; V_N^{(AB)}\,.$$

The choice of the scaled potentials depends also on the space dimension. For concreteness, a family of possible scalings in $d = 3$ dimensions is

$$V_N(\mathbf{x}) \;=\; N^{3\beta-1}V(N^\beta\mathbf{x})\,, \qquad \beta\in[0,1]\,, \tag{22}$$

which includes the *mean field* ($\beta = 0$) and the *Gross-Pitaevskii* ($\beta = 1$) scalings: they all guarantee that kinetic and potential energy in a sufficiently generic many-body state keep a constant ratio in the limit, that is, the dynamics remains non-trivial also when $N \to \infty$. They also have various degree of realism: the larger the β in $(0, 1]$, the more realistic the interaction, in the sense that V_N has a short scale and strong magnitude. Moreover, it can be seen that (22) for $\beta \in (0, 1]$ defines a potential whose scattering length a_N scales as $a_N \sim N^{-1}$, while the mean density of the gas scales as $\rho_N \sim N$, whence $\rho_N a_N^3 \sim N^{-2} \to 0$, which is a limit of high dilution: $\rho_N a_N^3$ is indeed the cube of the ratio between the scattering length a_N and the mean inter-particle distance $\rho_N^{-1/3}$. We recall that for fairly general interactions and trapping potentials the ground state energy per particle $e_0 := \lim_{N\to\infty} N^{-1}E_{\text{g.s.}}(N, a)$ of a Bose gas *in the thermodynamic limit* in three dimensions, with density ρ and inter-particle scattering length a, is given by

$$e_0 \;=\; \frac{2\pi\hbar^2}{m}\,\rho a\,(1+O((\rho a^3)^\nu)) \qquad \text{as}\;\; \rho a^3\to 0 \tag{23}$$

for some constant $\nu \in (0, 1)$: thus, replacing the actual thermodynamic limit as $N \to \infty$ with the scaling $\rho_N \sim N$, $a_N \sim N^{-1}$ has the feature of yielding the same physical asymptotics $\frac{2\pi\hbar^2}{m}\rho_N a_N$ in the r.h.s. of (23). The gain is a doable analysis of the limits

$\lim_{N\to\infty} N^{-1}E_{\rm gs}(N,a_N)$ and $\lim_{N\to\infty}\gamma_N^{(1)}$: indeed, it is in this scaling that for a one-component Bose gas in a three-dimensional trap, complete BEC was proved in the sense of (8) [30, Section 6.1].

Analogous considerations can be made for scaling limits in $d=2$ dimensions: we defer the discussion of this case to Subsection 3.5 below.

3.4. Emergence of effective cubic coupled NLS: the three-dimensional case

Within the conceptual scheme presented so far, a recent stream has started on the rigorous derivation of the effective dynamics of mixtures of condensate. Recent results by one of us in collaboration with A. Olgiati [37, 44] yield the following.

Theorem 3.1 (informal version)**.** *There is a class of suitable (physically realistic and non-restrictive) three-dimensional interaction potentials $V^{(A)}$, $V^{(B)}$, and $V^{(AB)}$ (which includes smooth and compactly supported potentials, as well as the Coulomb potential) for which the following holds.*

Consider the (self-adjoint) Hamiltonian H_{N_1,N_2} defined in (12) with such potentials and make a Gross-Pitaevskii rescaling, i.e., make the potentials N_1,N_2-dependent according to

$$\begin{aligned} V^{(A)}_{N_1}(\mathbf{x}) &= N_1^2\,V^{(A)}(N_1\mathbf{x}) \\ V^{(B)}_{N_2}(\mathbf{y}) &= N_2^2\,V^{(B)}(N_2\mathbf{y}) \\ V^{(AB)}_{N_1,N_2}(\mathbf{z}) &= (N_1+N_2)^2\,V^{(AB)}((N_1+N_2)\mathbf{z})\,. \end{aligned} \tag{24}$$

Assume non-zero population ratios c_1 and c_2, where $c_j := \lim_{N_1,N_2\to\infty}\frac{N_j}{N_1+N_2}$, $j=1,2$.

Let the system be prepared in the many-body state Ψ_{N_1,N_2} and assume that this is a state of binary condensation respectively on the one-particle orbitals u_0 and v_0. That is, $\Psi_{N_1,N_2}\in\mathcal{H}_{N_1,N_2,\rm sym}$ with $\|\Psi_{N_1,N_2}\|=1$, and there are $u_0,v_0\in L^2(\mathbb{R}^3)$ (taken in a suitably large class of regularity and integrability) with $\|u_0\|=\|v_0\|=1$ such that

$$\lim_{N_1,N_2\to\infty}\gamma^{(1,1)}_{N_1,N_2} \;=\; |u_0\otimes v_0\rangle\langle u_0\otimes v_0|\,. \tag{25}$$

Here $\gamma^{(1,1)}_{N_1,N_2}$ is the double reduced density matrix associated with Ψ_{N_1,N_2}, as in (14).

In addition, assume that the energy per particle $N^{-1}\langle\Psi_{N_1,N_2},H_{N_1,N_2}\Psi_{N_1,N_2}\rangle$ is given, asymptotically in N, by the minimum of the so-called Gross-Pitaevskii energy functional associated with the above potentials [44].

Let $\Psi_{N_1,N_2}(t) := e^{-\mathrm{i}\,t/\hbar\,H_{N_1,N_2}}\,\Psi_{N_1,N_2}$ be the solution to the corresponding Cauchy problem (17) for the many-body Schrödinger equation with initial datum Ψ_{N_1,N_2}.

Then at later times, more precisely for any t in the interval of existence of a solution of the system (27), the state $\Psi_{N_1,N_2}(t)$ preserves binary condensation in the sense that for the associated reduced density matrix $\gamma^{(1,1)}_{N_1,N_2}(t)$ there exist $u(t),v(t)\in L^2(\mathbb{R}^d)$, with $\|u(t)\|=\|v(t)\|=1$, such that

$$\lim_{N_1,N_2\to\infty}\gamma^{(1,1)}_{N_1,N_2}(t) \;=\; |u(t)\otimes v(t)\rangle\langle u(t)\otimes v(t)|\,. \tag{26}$$

The one-body orbitals $u(t)$ and $v(t)$ are the unique solutions to the following system of coupled cubic non-linear Schrödinger equations

$$\begin{aligned} \mathrm{i}\hbar\,\partial_t u &= -\tfrac{\hbar^2}{2m_A}\Delta u + Uu + \tfrac{4\pi\hbar^2 a_A}{m_A}|u|^2 u + c_2\tfrac{4\pi\hbar^2 a_{AB}}{m_{AB}}|v|^2 u \\ \mathrm{i}\hbar\,\partial_t v &= -\tfrac{\hbar^2}{2m_B}\Delta v + Uv + \tfrac{4\pi\hbar^2 a_B}{m_A}|v|^2 v + c_1\tfrac{4\pi\hbar^2 a_{AB}}{m_{AB}}|u|^2 v \end{aligned} \tag{27}$$

with initial data $u(0) = u_0$ and $v(0) = v_0$. Here a_A, a_B, and a_{AB} are the s-wave scattering lengths respectively of the three original (unscaled) potentials, $m_{AB} = \frac{m_A m_B}{m_A + m_B}$.

The evolution equations (27) emerging in this derivation are referred to as *Gross-Pitaevskii equations*. They provide an *effective* description of the dynamics, in the sense that $\Psi_{N_1,N_2}(t) \approx u(t)^{\otimes N_1} \otimes v(t)^{\otimes N_2}$ only holds at the level of reduced density matrices. In this weak, yet fully meaningful sense, one has a tremendous drop of complexity, for a *many-body* partial differential equation is reduced to two *one-particle* equations, one for each component, at the price of passing from a *linear* to a *non-linear* problem.

The cubic non-linearities have a natural interpretation of self-interaction terms: each of the two orbitals u and v is subject to effective potentials that are proportional to their densities: the term $|u|^2 u$ accounts for the self-interaction of an A-particle with the others of its species, $|u|^2 v$ for the interaction of an A-particles with the cloud of B-particles, etc. The factors c_1 and c_2 adjust the magnitude of each inter-species self-interaction term with respect to the the relative weights of each population.

Moreover, for dilute and weakly interacting Bose gases, (27) turn out to be well validated in the experiments – see [19, Section 16.2.1] for a concise review.

Theorem 3.1 can be visualized as follows:

$$\begin{array}{ccccc} \Psi_{N_1,N_2} & \xrightarrow{\text{partial trace}} & \gamma^{(1,1)}_{N_1,N_2} & \xrightarrow{N\to\infty} & |u_0\otimes v_0\rangle\langle u_0\otimes v_0| \\ \Big\downarrow{\scriptstyle \substack{\text{many-body}\\ \textbf{linear}\text{ dynamics}}} & & \Big\downarrow & & \Big\downarrow{\scriptstyle \substack{\textbf{nonlinear}\\ \text{Schrödinger eq.}}} \\ \Psi_{N_1,N_2}(t) & \longrightarrow & \gamma^{(1,1)}_{N_1,N_2}(t) & \xrightarrow{N\to\infty} & |u(t)\otimes v(t)\rangle\langle u(t)\otimes v(t)| \end{array} \tag{28}$$

In fact additional quantitative bounds, that we did not include here, are known on $\|\gamma^{(1,1)}_{N_1,N_2}(t) - |u(t)\otimes v(t)\rangle\langle u(t)\otimes v(t)|\|$ in terms of N_1, N_2, t. The very same type of theorem has been obtained in many guises and through several alternative mathematical techniques for Bose gases with *simple condensation* (see, e.g., the review in [8]). The already cited recent works [37, 44] have provided a first generalisation to the *multi-component* case.

It is worth emphasizing, however, that it is the rigorous derivation provided by Theorem 3.1 to be novel, whence our choice to review it in this Subsection, whereas the equations themselves are since long known to provide an effective "mean-field-like" solution to the many-body problem. In first quantisation this may be seen by evaluating the energy functional $\langle \Psi_{N_1,N_2}(t), H_{N_1,N_2}\Psi_{N_1,N_2}(t)\rangle$ with the formal Ansatz $\Psi_{N_1,N_2}(t) \equiv u(t)^{\otimes N_1} \otimes v(t)^{\otimes N_2}$ in the limit $N_1, N_t \to \infty$: an effective functional of u and v emerges, whose Euler-Lagrange equations are precisely (27) [37, Section 4]. In second quantisation the same can be seen by replacing the field operator with an order parameter and the actual potentials with delta-like pseudo-potentials of the form $V(\mathbf{x}) = \frac{4\pi\hbar^2 a}{m}\delta(\mathbf{x})$ [50, Chapters 5 and 21].

3.5. Two-dimensional analog

The non-linear system (27) describes the effective dynamics also for a two-dimensional binary condensate and its derivation from the many-body Schrödinger dynamics falls within the very same scheme discussed in Subsection 3.3 and visualized in (28). Analogously to the three-dimensional case, no control is known in a proper thermodynamic limit on the marginal $\gamma^{(1,1)}_{N_1,N_2}(t)$, so one investigates the asymptotics of this marginal as $N_1, N_2 \to \infty$ (in the sense or (21)) along a scaling limit that brings enough simplification while retaining relevant physical features.

The well-known peculiarity of the case $d = 2$ is that, unlike (23), the energy per particle of a dilute two-dimensional Bose gas is *non-linear* in the density ρ and takes the expression

$$e_0 \;=\; \frac{2\pi\hbar^2}{m}\,\rho\,|\ln(\rho a^2)|^{-1}\,(1+O(|\ln(\rho a^2)|^{-\nu}))\qquad \text{as}\;\; \rho a^2\to 0 \tag{29}$$

for some constant $\nu \in (0, 1)$, where a is the scattering length of the interaction. The dilution parameter ρa^2 equals the square of the ratio between the scattering length a and the mean inter-particle distance $\rho^{-1/2}$.

Thus, for a gas with N bosons in $\mathbb{R}^2$, letting $N \to \infty$ makes the mean density scale as $\rho_N \sim N$, and in order to match the same asymptotic value of the energy per particle given by (29) one has to re-scale the interaction so as $|\ln(\rho_N a_N^2)| \sim N$. This is the two-dimensional analog of the Gross-Pitaevskii limit:

$$\rho_N\,|\ln(\rho_N a_N^2)|^{-1} \;=\; \text{const.}\qquad (d=2)\,, \tag{30}$$

as opposed to $\rho_N a_N = \text{const.}$ when $d = 3$. It is in this scaling that for a one-component Bose gas in a two-dimensional trap, complete BEC was proved in the sense of (8) [30, Section 6.2].

Besides (30), it is still meaningful to adopt also for $d = 2$ one of the scalings

$$V_N(\mathbf{x}) \;=\; N^{3\beta-1}V(N^\beta\mathbf{x})\,,\qquad \beta\in[0,1] \tag{31}$$

considered for $d = 3$, because, again, in the limit $N \to \infty$ they all guarantee a formal balance between kinetic and potential energy, and hence a non-trivial dynamics. However, one can see that for $\beta \in (0, 1]$ the scattering length of the potential V_N given by (31) scales as $a_N \sim N^{-1}$, whence $e_0 \sim \rho_N\,|\ln(\rho_N a_N^2)|^{-1} \sim N(\ln N)^{-1} \to \infty$ (a_N should instead vanish exponentially with N in order to keep the quantity $\rho_N\,|\ln(\rho_N a_N^2)|^{-1}$ constant as in the Gross-Pitaevskii scaling).

Whether (30), or (31) with $\beta \in (0, 1]$, is the most appropriate scaling is a matter of which physical feature one wants to retain in the limit. The former keeps the re-scaled thermodynamic ground state energy per particle constant, while the latter instead makes it non-physically diverge; on the other hand, the quantity $\rho|\ln(\rho a^2)|^{-1}$ is indeed typically *very large* in two dimensional experiments, and therefore the scaling $\rho_N\,|\ln(\rho_N a_N^2)|^{-1} \to \infty$, $\rho_N a_N^2 \to 0$ retains an amount of physical relevance.

Concerning the rigorous derivation of the effective dynamics of a two-dimensional condensate, no result is known in the scaling (30): in the one-component case, the cubic

non-linear Schrödinger equation was derived in the scaling (31) first in [24], and in the scaling (30) first in [21]. By means of the same technique that yields the non-linear system (27) these derivations are exportable to the two-component case.

4. Coupled system of NLS in 2D: well-posedness and other features

The system of coupled non-linear Schrödinger (Gross-Pitaevskii) equations of interest, re-written in suitable units and with the explicit dependence on the population ratios, reads

$$\begin{aligned} \mathrm{i}\,\partial_t u &= -\Delta u + Uu + \gamma_1|u|^2u + c_2\gamma_{12}|v|^2u \\ \mathrm{i}\,\partial_t v &= -\Delta v + Uv + \gamma_2|v|^2v + c_1\gamma_{12}|u|^2v\,, \end{aligned} \tag{32}$$

where γ_α, $\alpha \in \{1, 2, 12\}$, are the intra-species and inter-species scattering lengths and c_1, c_2 are the two population weights.

Here the unknowns are the functions $u \equiv u(\mathbf{x}, t)$ and $v \equiv v(\mathbf{x}, t)$ with $\mathbf{x} \in \mathbb{R}^2$ and $t \in [0, T]$ for some $T \in (0, +\infty]$ that determines the time interval of existence of the solution. As customary, by H^1-solution of (32) we shall mean a couple (u, v) with $u, v \in C([0, T], H^1(\mathbb{R}^2))$.

Two quantities conserved in time for H^1-solutions to (32) are the total mass

$$\mathcal{M}[u, v] := (\tfrac{c_1}{c_2}\|u\|_2^2 + \|v\|_2^2)^{1/2} \tag{33}$$

and the total energy

$$\mathcal{E}[u, v] := \mathcal{K}[u, v] + \mathcal{U}[u, v] + \mathcal{P}[u, v]\,, \tag{34}$$

where

$$\mathcal{K}[u, v] := \frac{1}{2}\frac{c_1}{c_2}\|\nabla u\|_2^2 + \frac{1}{2}\|\nabla v\|_2^2 \tag{35}$$

$$\mathcal{U}[u, v] := \frac{1}{2}\frac{c_1}{c_2}\int_{\mathbb{R}^2} U|u|^2\mathrm{d}\mathbf{x} + \frac{1}{2}\int_{\mathbb{R}^2} U|v|^2\mathrm{d}\mathbf{x} \tag{36}$$

$$\mathcal{P}[u, v] := \frac{1}{4}\gamma_1\frac{c_1}{c_2}\|u\|_4^4 + \frac{1}{4}\gamma_2\|v\|_4^4 + \frac{c_1}{2}\gamma_{12}\int_{\mathbb{R}^2} |u|^2|v|^2\mathrm{d}\mathbf{x} \tag{37}$$

In fact, also the masses $\|u\|_2$ and $\|v\|_2$ of each component are also conserved *separately*.

Further relevant quantities are

$$\Sigma[u, v] := \frac{c_1}{c_2}\||x|u\|_2^2 + \||x|v\|_2^2\,, \tag{38}$$

$$\mathcal{G}[u, v] := \mathcal{M}[u, v]^2 + \mathcal{P}[u, v]\,, \tag{39}$$

$$\mathcal{R}[u, v] := \mathfrak{Im}\int_{\mathbb{R}^2}\Big(\frac{c_1}{c_2}\,\overline{u}\,\mathbf{x}\cdot\nabla u + \overline{v}\,\mathbf{x}\cdot\nabla v\Big)\,\mathrm{d}\mathbf{x}\,. \tag{40}$$

As long as all the interactions of the model are *repulsive*, meaning $\gamma_1 > 0$, $\gamma_2 > 0$, and $\gamma_{12} > 0$, (32) consists of two coupled *de-focusing* cubic non-linear Schrödinger equations with a unique global-in-time H^1-solution (i.e., $T = \infty$) – which can be seen by adapting the same well-established analysis for one single NLS [11]. However, in

two spatial dimensions the cubic non-linearities of (32) are energy-critical and, in the presence of attracting interactions, finite-time blow-up of the H^1-norm may occur.

A wide literature is available on the well-posedness of the system (32). In the following Subsections we review the main typical phenomena.

4.1. General regimes of global well-posedness

The system (32) is well-posed in H^1 globally in time whenever the interactions are all repulsive or the initial data have a sufficiently small mass. For example, the following is known ([22]).

Let

$$U(\mathbf{x}) \;=\; \omega^2\,|\mathbf{x}|^2 \qquad (\omega>0) \tag{41}$$

and assume that the initial data satisfy

$$u_0, v_0 \;\in\; H^1(\mathbb{R}^2) \qquad \text{and} \qquad \Sigma[u_0,v_0] \;<\; +\infty\,. \tag{42}$$

Then in any of the following four cases, the Cauchy problem associated with the system (32) has a unique solution (u,v) with $u,v\in C([0,+\infty),H^1(\mathbb{R}^2))$:

$$\begin{array}{ll}
\text{(i)} & \gamma_1,\gamma_2,\gamma_{12}\geqslant 0\,,\\
\text{(ii)} & \gamma_1,\gamma_2\geqslant 0\,,\ \gamma_{12}<0\,,\ \mathcal{M}[u_0,v_0]<2\|Q\|_2|\gamma_{12}|^{-\frac{1}{2}}\,,\\
\text{(iii)} & \gamma_1,\gamma_2<0\,,\ \gamma_{12}>0\,,\ \mathcal{M}[u_0,v_0]<\|Q\|_2(\max\{|\gamma_1|,|\gamma_2|\})^{-\frac{1}{2}}\,,\\
\text{(iv)} & \gamma_1,\gamma_2,\gamma_{12}<0\,,\ \mathcal{M}[u_0,v_0]<\|Q\|_2\Big(\frac{8}{4\max\{|\gamma_1|,|\gamma_2|\}+|\gamma_{12}|}\Big)^{\frac{1}{2}}.
\end{array} \tag{43}$$

Here Q is the ground state solution to

$$-\Delta Q + Q + Q^3 \;=\; 0\,. \tag{44}$$

4.2. General regimes of blow-up

The following is known ([22]). Let

$$U(\mathbf{x}) \;=\; \omega^2\,|\mathbf{x}|^2 \qquad (\omega>0) \tag{45}$$

and assume that the initial data satisfy

$$u_0, v_0 \;\in\; H^1(\mathbb{R}^2) \qquad \text{and} \qquad \Sigma[u_0,v_0] \;<\; +\infty \tag{46}$$

and one of the two conditions

$$\begin{array}{ll}
\text{(C1)} & \mathcal{E}[u_0,v_0] \;<\; 2\,\omega^2\,\Sigma[u_0,v_0]\,,\\
\text{(C2)} & \mathcal{R}[u_0,v_0] \;<\; 0 \quad\text{and}\quad \mathcal{E}[u_0,v_0]<-\omega\mathcal{R}[u_0,v_0]\,.
\end{array} \tag{47}$$

Assume also that the couplings of the non-linearities belong to one of the four regimes

$$\begin{array}{ll}
\text{(i)} & \gamma_1,\gamma_2\geqslant 0\,,\ \gamma_{12}<0\,,\\
\text{(ii)} & \gamma_1\geqslant 0\,,\ \gamma_2<0\,,\\
\text{(iii)} & \gamma_1<0\,,\ \gamma_2\geqslant 0\,,\\
\text{(iv)} & \gamma_1,\gamma_2<0\,.
\end{array} \tag{48}$$

Then there exists a finite blow-up time $T^* > 0$ such that

$$\lim_{t\uparrow T^*}(\|\nabla u\|_2^2 + \|\nabla v\|_2^2) \;=\; +\infty\,, \tag{49}$$

and

$$T^* \leqslant \frac{\pi}{4\omega} \quad \text{in case (C1)}\,, \qquad T^* \leqslant \frac{\pi}{8\omega} \quad \text{in case (C2)}\,. \tag{50}$$

4.3. Blow-up thresholds for the inter-species attraction (focusing) regime

The following is known ([32]). Assume

$$U \equiv 0\,, \qquad \gamma_1 < 0\,, \qquad \gamma_2 < 0\,, \tag{51}$$

and

$$\gamma_{12} \;<\; 0 \qquad \text{or} \qquad \begin{cases} \gamma_{12} \;>\; 0 \quad \text{and} \\ c_1c_2\gamma_{12}^2 \;<\; \gamma_1\gamma_2\,. \end{cases} \tag{52}$$

Then $\mathcal{P}[u,v] < 0$ for $u, v \in H^1(\mathbb{R}^2)\setminus\{\mathbf{0}\}$ and the variational problem

$$\kappa \;:=\; \inf_{\substack{u,v\in H^1(\mathbb{R}^2)\\(u,v)\neq(\mathbf{0},\mathbf{0})}} \frac{\mathcal{K}[u,v]\,\mathcal{M}[u,v]^2}{-\mathcal{P}[u,v]} \tag{53}$$

satisfies $\kappa > 0$. If the initial data satisfy the smallness condition

$$\mathcal{M}[u_0,v_0]^2 + \mathcal{E}[u_0,v_0] \;<\; \kappa\,, \tag{54}$$

then:

(i) if $\mathcal{G}[u_0,v_0] > 0$, then (32) is globally-in-time well-posed in H^1,

(ii) if $\mathcal{G}[u_0,v_0] < 0$ and $\Sigma[u_0,v_0] < +\infty$, then (32) has a unique solution in H^1 locally in time, for which $\|\nabla u\|_2^2 + \|\nabla v\|_2^2$ blows up in finite time.

In fact, the blow-up threshold is intimately related to the ground state solution of the stationary problem corresponding to (32), as the following results show [18, 29]. Let

$$U \;\equiv\; 0 \qquad \text{and} \qquad \gamma_1 = \gamma_2 = -1\,, \quad c_1 = c_2 = \tfrac{1}{2}\,, \tag{55}$$

and assume that the initial data satisfy

$$u_0, v_0 \;\in\; H^1(\mathbb{R}^2) \qquad \text{and} \qquad \Sigma[u_0,v_0] \;<\; +\infty\,. \tag{56}$$

Let (Q,R) be a ground state solution to

$$\begin{aligned} -\Delta Q + Q - |Q|^2Q + \tfrac{1}{2}\gamma_{12}|R|^2Q \;&=\; 0 \\ -\Delta R + R - |R|^2R + \tfrac{1}{2}\gamma_{12}|Q|^2R \;&=\; 0\,. \end{aligned} \tag{57}$$

Then:

(i) If $\mathcal{E}[u_0,v_0] \;<\; 0$, then (32) has a unique local-in-time H^1-solution for which $\|\nabla u\|_2^2 + \|\nabla v\|_2^2$ blows up in finite time.

(ii) If $\mathcal{E}[u_0, v_0] > 0$ and $\mathcal{M}[u_0, v_0]$ is sufficiently large, precisely

$$\|u_0\|_2^2 + \|v_0\|_2^2 \;>\; \|Q\|_2^2 + \|R\|_2^2\,, \tag{58}$$

then (32) has a unique local-in-time H^1-solution for which $\|\nabla u\|_2^2 + \|\nabla v\|_2^2$ blows up in finite time.

(iii) There are initial data for which

$$\|u_0\|_2^2 + \|v_0\|_2^2 \;=\; \|Q\|_2^2 + \|R\|_2^2\,, \tag{59}$$

such that (32) has a unique local-in-time H^1-solution for which $\|\nabla u\|_2^2 + \|\nabla v\|_2^2$ blows up in finite time.

(iv) If $\mathcal{E}[u_0, v_0] > 0$ and $\mathcal{M}[u_0, v_0]$ is sufficiently small, precisely

$$\|u_0\|_2^2 + \|v_0\|_2^2 \;<\; \|Q\|_2^2 + \|R\|_2^2\,, \tag{60}$$

then (32) is globally-in-time well-posed in H^1.

4.4. Inter-species focusing: simultaneous blow-up

The following is known ([31, 14]). Assume conditions (51) and assume also that the initial data satisfy

$$u_0, v_0 \;\in\; H^1(\mathbb{R}^2) \qquad \text{and} \qquad \Sigma[u_0, v_0] \;<\; +\infty\,, \tag{61}$$

and one of the three conditions

$$\begin{aligned} &\text{(C1)} \quad \mathcal{E}[u_0, v_0] \;<\; 0\,, \\ &\text{(C2)} \quad \mathcal{E}[u_0, v_0] \;=\; 0 \quad \text{and} \quad \mathcal{R}[u_0, v_0] \;<\; 0\,, \\ &\text{(C3)} \quad \mathcal{E}[u_0, v_0] \;>\; 0 \quad \text{and} \quad \mathcal{R}[u_0, v_0] \;\leqslant\; -\sqrt{8\,\mathcal{E}[u_0, v_0]\cdot\Sigma[u_0, v_0]}\,. \end{aligned} \tag{62}$$

Then there exists a finite time of simultaneous blow-up $T^* > 0$ such that

$$\lim_{t\uparrow T^*} \|\nabla u\|_2 \;=\; \lim_{t\uparrow T^*} \|\nabla v\|_2 \;=\; +\infty \tag{63}$$

and furthermore

$$\text{either} \quad \lim_{t\uparrow T^*} \|u\|_\infty \;=\; +\infty \qquad \text{or} \quad \lim_{t\uparrow T^*} \|v\|_\infty \tag{64}$$

provided that $(u_0, v_0) \neq (\mathbf{0}, \mathbf{0})$.

5. Numerical analysis: outlook on the recent literature

The two-dimensional Gross-Pitaevskii non-linear system (32), together with certain generalisations of it, is the object of extensive numerical studies, both for its physical relevance and as a playground for testing alternative numerical techniques. Let us surf here the pertinent works in the previous literature, also with the aim of highlighting the main novelties of our numerics.

5.1. Single component

For a *single-component* Gross-Pitaevskii equation, a variety of numerical methods have been introduced over the last decade, which include *time-splitting pseudo-spectral methods* (also known as *collocation methods*) based on Fourier, spherical harmonics, and Laguerre-Hermite basis functions, as well as *Laguerre spectral methods*.

Bao, Jaksch, and Markowich [6] and Bao and Jaksch [5] proposed a second order Strang splitting combined with a Fourier collocation method in time (TSSP). They apply it to the 1D and 2D problem, where TSSP shows indeed second order convergence in time and spectral convergence in space, as opposite to the Crank-Nicholson time discretisation, that fails to achieve second order convergence in 1D, and whose implicit step hinders spectral accuracy in space in 2D. In 3D and with radially or cylindrically symmetric trapping potential, Bao and Shen [7] proposed a Laguerre-Hermite pseudo-spectral method with a fourth-order splitting in time.

An application of the conservative Crank-Nicolson finite difference method to the single Gross-Pitaevskii equation was proposed by Ruprecht et al. [51]. This algorithm is stable and unitary (i.e., L^2-norm preserving) for any time step size, meaning that numerical errors do not grow in time; however, the non-linear coupling between different vibrational modes may make even tiny random-noise perturbations in the wave-function result in a proper excitation of the condensate with injection of extra kinetic energy, which creates a limit to the numerical stability of the method.

Cerimele et al. [13, 12] introduced a finite difference method based on an adaptation of the explicit, time-staggered scheme proposed by Visscher to solve the Schrödinger equation in an external potential, and they validated unitarity and stability when the non-linearity is added.

An adaptation of the local one-dimensional multi-symplectic scheme to the three-dimensional Gross-Pitaevskii equation has been proposed by Kong, Hong, and Zhang [26] exploiting the advantage of multi-symplectic integrators and the cheap computational cost of the local one-dimensional method, and it revealed satisfactory conservation of mass and energy in the special case of a wave-function with separated variables. This method provides an order 2.5 in space and is slightly above 2 in time.

For the dynamics of *rotating* condensates, namely when an angular momentum term is added to the Gross-Pitaevskii equation, pseudo-spectral methods encounter serious limitations. In polar coordinates, Bao, Du, and Zhang [4] proposed a hybrid method based on a second order finite element discretisation in the radial direction and a Fourier pseudo-spectral method in the angular direction, coupled with a Strang splitting in time. This method is extended to the 3D case with cylindrical coordinates by combining a finite element method for the radial direction, the Fourier pseudo-spectral method in the angular direction, and a sine pseudo-spectral method for the axial coordinate.

For a comprehensive review of the above-mentioned numerical methods applied to the Gross-Pitaevskii dynamics we refer to [3, Section 4].

5.2. Multiple components

In application to *multi-component* BEC, the TSSP method was used first by Bao [2] (explicitly only in 1D) for a modification of the non-linear system (32) which includes also linear coupling terms that account for a transition between the two populations, induced by an external field – a setting not included in our present analysis, but that can cover also the system (32) itself.

Xu and Chang [56] proposed two second order split-step methods using both fourth order finite differences and a Fourier pseudo-spectral method in space for the study of soliton solutions of the 1D analog of the non-linear system (32)

When both equations of (32) are supplemented with an angular momentum term, the resulting system models a two-component *rotating* condensate, another setting that we do not cover here, having it already received a considerable amount of attention in the literature [57, 52, 38, 55]. In particular, Zhang, Bao, and Li [57] studied this system in cylindrical coordinates using a fourth-order finite difference method in the radial direction, a Fourier pseudo-spectral method in the angular direction, and a sine pseudo-spectral method in the axial direction, with an advance in time obtained both with a Strang splitting and with a Crank-Nicholson scheme. More recently, Salman [52] studied both one- and two-component BEC with an external (harmonic or toric) potential in polar and spherical coordinates using the Fourier or the spherical harmonics pseudo-spectral method in the angular directions, coupled with a generalised spectral Laguerre method in the radial direction: both in 2D and in 3D a second order Strang splitting in time is adopted, and so is done by White, Hennessy, and Bush in [55].

5.3. Collisions of condensates: quest for high resolution and parallel computing

In the above-mentioned works, the phenomena simulated in the computations are mainly of the following types: "free" relaxation of a single condensate (namely, one Gross-Pitaevskii with no confining potential, modelling a condensate that expands ballistically after the trap is removed), solitons propagating in a single or multi-condensate, and rotating condensates.

All such computations turn out to be quite manageable numerically, favoured by the fact that the considered phenomena do not involve a *complicated collision interaction* between spatially well-localised components. Thus, among the already cited works, the 2D maximum resolution of [52] is given by a 96×96 grid (and $96 \times 64 \times 32$ in 3D), which becomes 200×256 in [57], 256×256 in [2], and 1024×128 in [4]. Furthermore, only [2] and [4] achieve spectral accuracy in *all* space directions.

Remarkably, a systematic numerics of various types of collisions between the condensate components, including symmetric and asymmetric collisions followed by ballistic expansion, as well as repeated collisions in a trap, is missing in the literature. We fill in precisely this gap in Sections 6 and 7 below.

To this aim, however, the standard resolution adopted in the previous works is insufficient and parallel computation is required, in order to resolve relevant short-

scale details of the dynamics. With our numerical code we shall implement MPI parallel simulations in which we have no difficulties to reach resolutions of magnitude 16384×16384.

6. Numerical analysis: methods

For the numerical solution of the initial value problem associated with the system (32) we choose a Fourier collocation method [10] in space (sometimes called Fourier pseudo-spectral method) combined with an integrating factor method in time.

6.1. Space discretisation

As customary, we work with (a suitably discretised version of) the system (32) re-written after a Fourier transform in space as

$$\begin{aligned} \mathrm{i}\partial_t \widehat{u} &= \mathbf{L}\widehat{u} + \mathbf{N}_v(\widehat{u}) \\ \mathrm{i}\partial_t \widehat{v} &= \mathbf{L}\widehat{v} + \mathbf{N}_u(\widehat{v}), \end{aligned} \tag{65}$$

where we set $\mathbf{L} := \mathbf{k}^2$, we denoted the linear and non-linear parts of the equations as

$$\begin{aligned} \mathbf{L}\widehat{u} &= \mathbf{k}^2\widehat{u} \\ \mathbf{N}_v(\widehat{u}) &:= \widehat{Uu} + \gamma_1\widehat{|u|^2 u} + c_2\gamma_{12}\widehat{|v|^2 u} \\ \mathbf{N}_u(\widehat{v}) &:= \widehat{Uv} + \gamma_2\widehat{|v|^2 v} + c_1\gamma_{12}\widehat{|u|^2 v}\,, \end{aligned} \tag{66}$$

and where the convention

$$\widehat{f}(\mathbf{k}) := \frac{1}{2\pi}\int_{\mathbb{R}^2} \mathrm{e}^{-\mathrm{i}\mathbf{k}\cdot\mathbf{x}} f(\mathbf{x})\mathrm{d}\,\mathbf{x} \tag{67}$$

is adopted for the Fourier transform.

The spatial domain for both $u(\mathbf{x},t)$ and $v(\mathbf{x},t)$, with $\mathbf{x} \equiv (x,y) \in \mathbb{R}^2$, is taken to be the square $I \times I$ with $I := [-\pi, \pi]$; periodic boundary conditions are assumed (that is, the underlying Hilbert space is that of L^2-functions on the corresponding torus) and the Fourier transform (67) is discretized accordingly.

On each interval I we consider a grid of N equispaced points ($N =$ a power of 2, for convenience), thus resulting in a regular square lattice of N^2 points, on which we implement a Fourier collocation method by replacing $u(\mathbf{x},t)$ and $v(\mathbf{x},t)$ with a suitable truncation of their Fourier series representation, namely

$$\begin{aligned} u(\mathbf{x},t) &\approx \sum_{k_x,k_y=-N/2+1}^{N/2} \widehat{u}_{k_x,k_y}(t)\,\mathrm{e}^{\mathrm{i}k_x x}\mathrm{e}^{\mathrm{i}k_y y} \\ v(\mathbf{x},t) &\approx \sum_{k_x,k_y=-N/2+1}^{N/2} \widehat{v}_{k_x,k_y}(t)\,\mathrm{e}^{\mathrm{i}k_x x}\mathrm{e}^{\mathrm{i}k_y y}\,. \end{aligned} \tag{68}$$

We then require the truncated series (68) to satisfy the system (32) at the collocation points, proceeding as follows. First, from the knowledge of the numerical sequences

$$(\widehat{u}_{k_x,k_y}(t))_{k_x,k_y=-\frac{N}{2}+1}^{\frac{N}{2}} \qquad \text{and} \qquad (\widehat{v}_{k_x,k_y}(t))_{k_x,k_y=-\frac{N}{2}+1}^{\frac{N}{2}}\,,$$

which are going to become our actual unknowns, one reconstructs by means of (68) the approximated $u(\mathbf{x},t)$ and $v(\mathbf{x},t)$. Then one computes, on the points of the spatial grid, the corresponding non-linearities and, in analogy to (68), one expresses them in their (truncated) Fourier representation

$$\begin{aligned}(Uu+\gamma_1|u|^2u+c_2\gamma_{12}|v|^2u)(\mathbf{x},t) &\approx \sum_{k_x,k_y=-N/2+1}^{N/2} \mathcal{N}^{(1)}_{k_x,k_y}(t)\,\mathrm{e}^{\mathrm{i}k_xx}\mathrm{e}^{\mathrm{i}k_yy}\\ (Uv+\gamma_2|v|^2v+c_1\gamma_{12}|u|^2v)(\mathbf{x},t) &\approx \sum_{k_x,k_y=-N/2+1}^{N/2} \mathcal{N}^{(2)}_{k_x,k_y}(t)\,\mathrm{e}^{\mathrm{i}k_xx}\mathrm{e}^{\mathrm{i}k_yy}\,.\end{aligned} \tag{69}$$

Last, one plugs (68) and (69) into (32) and selects by orthogonality, for each (k_x,k_y), the (k_x,k_y)-component on both sides, so as to obtain, from the initial system (32) of two coupled NLS, the following system of $2N^2$ coupled non-linear ODEs:

$$\begin{aligned}\mathrm{i}\tfrac{\mathrm{d}}{\mathrm{d}t}\,\widehat{u}_{k_x,k_y} &= \mathbf{L}\widehat{u}_{k_x,k_y}+\mathcal{N}^{(1)}_{k_x,k_y}\\ \mathrm{i}\tfrac{\mathrm{d}}{\mathrm{d}t}\,\widehat{v}_{k_x,k_y} &= \mathbf{L}\widehat{v}_{k_x,k_y}+\mathcal{N}^{(2)}_{k_x,k_y}.\end{aligned} \tag{70}$$

(As well known, the computation of the non-linear terms of (70) by first inverse Fourier-transforming the $\widehat{u}_{k_x,k_y}$'s and $\widehat{v}_{k_x,k_y}$'s, computing the non-linearities on the spatial grid, and then Fourier-transforming back as in (69), has the virtue of avoiding the actual computation of convolutions in momentum space such as $\widehat{|u|^2u}=2\pi\widehat{|u|^2}*\widehat{u}$, thus reducing the computational cost from $O(N^2)$ to $O(N\log N)$.)

It is worth remarking that the Fourier collocation method sketched above in a Cartesian coordinate frame is in no way limited to a two-dimensional setting, and can be straightforwardly re-formulated for 1D or 3D problems.

6.2. Time discretisation

As in most time marching schemes, we consider $M+1$ instants $\{t^{(n)}\}_{n=0}^{M}$ within the time interval $[0,T]$, with $t^{(0)}=0$ and $t^{(M)}=T$, taking them for the present purposes to be equispaced with time step $h=t^{(n+1)}-t^{(n)}=T/M$, and we aim at evaluating approximately the Fourier coefficients $\widehat{u}_{k_x,k_y}(t)$ and $\widehat{v}_{k_x,k_y}(t)$ at each instant $t^{(n)}$.

From the knowledge of $\widehat{u}^{(n)}_{k_x,k_y}:=\widehat{u}_{k_x,k_y}(t^{(n)})$ and $\widehat{v}^{(n)}_{k_x,k_y}:=\widehat{v}_{k_x,k_y}(t^{(n)})$ at time $t^{(n)}$, the coefficients $\widehat{u}^{(n+1)}_{k_x,k_y}$ and $\widehat{v}^{(n+1)}_{k_x,k_y}$ at the subsequent time $t^{(n+1)}$ are approximated by the formulas

$$\begin{aligned}\widehat{u}^{(n+1)}_{k_x,k_y} &= \mathrm{e}^{-\mathrm{i}\mathbf{L}h}\widehat{u}^{(n)}_{k_x,k_y}-\mathrm{i}\mathrm{e}^{-\mathrm{i}\mathbf{L}h}\int_0^h \mathrm{e}^{\mathrm{i}\mathbf{L}\tau}\,\mathcal{N}^{(1)}_{k_x,k_y}(t^{(n+1)}-\tau)\,\mathrm{d}\tau\\ \widehat{v}^{(n+1)}_{k_x,k_y} &= \mathrm{e}^{-\mathrm{i}\mathbf{L}h}\widehat{v}^{(n)}_{k_x,k_y}-\mathrm{i}\mathrm{e}^{-\mathrm{i}\mathbf{L}h}\int_0^h \mathrm{e}^{\mathrm{i}\mathbf{L}\tau}\,\mathcal{N}^{(2)}_{k_x,k_y}(t^{(n+1)}-\tau)\,\mathrm{d}\tau\end{aligned} \tag{71}$$

which is precisely (70) formally re-written in integral forms. The integrals in (71) are then evaluated by quadratures by means of a *fourth order* OIFS4 scheme [9], a 4-stage

scheme that reads

$$\begin{aligned}
\mathcal{N}_0^{(j)} &= \mathcal{N}^{(j)}(\widehat{u}^{(n)}, \widehat{v}^{(n)}) \\
\mathcal{N}_1^{(j)} &= \mathcal{N}^{(j)}(\mathrm{e}^{-\mathrm{i}\mathbf{L}h/2}\widehat{u}^{(n)} + \tfrac{h}{2}\mathrm{e}^{-\mathrm{i}\mathbf{L}h/2}\mathcal{N}_0^{(1)}, \mathrm{e}^{-\mathrm{i}\mathbf{L}h/2}\widehat{v}^{(n)} + \tfrac{h}{2}\mathrm{e}^{-\mathrm{i}\mathbf{L}h/2}\mathcal{N}_0^{(2)}) \\
\mathcal{N}_2^{(j)} &= \mathcal{N}^{(j)}(\mathrm{e}^{-\mathrm{i}\mathbf{L}h/2}\widehat{u}^{(n)} + \tfrac{h}{2}\mathrm{e}^{-\mathrm{i}\mathbf{L}h/2}\mathcal{N}_1^{(1)}, \mathrm{e}^{-\mathrm{i}\mathbf{L}h/2}\widehat{v}^{(n)} + \tfrac{h}{2}\mathrm{e}^{-\mathrm{i}\mathbf{L}h/2}\mathcal{N}_1^{(2)}) \\
\mathcal{N}_3^{(j)} &= \mathcal{N}^{(j)}(\mathrm{e}^{-\mathrm{i}\mathbf{L}h}\widehat{u}^{(n)} + h\mathrm{e}^{-\mathrm{i}\mathbf{L}h/2}\mathcal{N}_2^{(1)}, \mathrm{e}^{-\mathrm{i}\mathbf{L}h}\widehat{v}^{(n)} + h\mathrm{e}^{-\mathrm{i}\mathbf{L}h/2}\mathcal{N}_2^{(2)})
\end{aligned} \tag{72}$$

and

$$\begin{aligned}
\widehat{u}_{k_x,k_y}^{(n+1)} &= \mathrm{e}^{-\mathrm{i}\mathbf{L}h}\widehat{u}_{k_x,k_y}^{(n)} - \mathrm{i}\mathrm{e}^{-\mathrm{i}\mathbf{L}h}\tfrac{h}{6}\Big(\mathcal{N}_0^{(1)} + 2\mathcal{N}_1^{(1)} + 2\mathcal{N}_2^{(1)} + \mathcal{N}_3^{(1)}\Big) \\
\widehat{v}_{k_x,k_y}^{(n+1)} &= \mathrm{e}^{-\mathrm{i}\mathbf{L}h}\widehat{v}_{k_x,k_y}^{(n)} - \mathrm{i}\mathrm{e}^{-\mathrm{i}\mathbf{L}h}\tfrac{h}{6}\Big(\mathcal{N}_0^{(2)} + 2\mathcal{N}_1^{(2)} + 2\mathcal{N}_2^{(2)} + \mathcal{N}_3^{(2)}\Big),
\end{aligned} \tag{73}$$

where $j \in \{1,2\}$ and $\mathcal{N}^{(j)} \equiv \mathcal{N}_{k_x,k_y}^{(j)}$.

In [9] the efficiency of several exponential time integrator schemes in the numerical propagation of the Schrödinger equation is compared, and for sufficiently regular potentials and initial data the OIFS4 scheme appears to be the most efficient.

6.3. Accuracy check

The accuracy of the numerical solution is controlled in two ways.

The first consists of checking the conservation of the mass (i.e., the L^2-norm) of each orbital separately (we discussed these conservation laws at the beginning of Section 4). We thus evaluate the relative discrepancies of $\|u_{\mathrm{num}}(\cdot,t)\|_2$ and of $\|v_{\mathrm{num}}(\cdot,t)\|_2$, where u_{num} and v_{num} denote the numerical solutions, with respect to their values at $t=0$. We fix the operational criterion to consider acceptable those solutions for which

$$\max\left\{\frac{|\,\|u_{\mathrm{num}}(\cdot,t)\|_2 - \|u_0\|_2\,|}{\|u_0\|_2}\,,\ \frac{|\,\|v_{\mathrm{num}}(\cdot,t)\|_2 - \|v_0\|_2\,|}{\|v_0\|_2}\right\} \ < \ 10^{-5}\,. \tag{74}$$

As an example of how this criterion is indeed well satisfied throughout our analysis, we plot in Figure 1 the above-mentioned relative errors for one of the numerical experiments discussed in Section 7.3, that is, the multiple re-collisions of a two-component condensate confined in a harmonic trap. The plot shows that the quantity in the l.h.s. of (74) increases in time, due to the unavoidable deterioration of the numerical precision, staying however three orders of magnitude below our fidelity threshold. The plateau-and-climb pattern corresponds to the alternating sequences of expansions of the two far apart condensates (plateaus) and spatial overlaps of the two components with strong interactions among them (climbs).

As a second accuracy criterion, we deem a solution acceptable as long as the magnitude of the high frequency Fourier modes does not exceed 10^{-6}. This is motivated by the fact that even when the initial datum is only given by a small amount of *low* frequency coefficients $\widehat{u}_{k_x,k_y}$'s and $\widehat{v}_{k_x,k_y}$'s (all the high frequency ones falling to the machine zero), as time advances the contribution of *high* (k_x,k_y) becomes more and more relevant, up to the point when even the highest frequencies considered in the truncation (68) give a non-negligible contribution. At this point essentially all Fourier coefficients with value comparable to the machine zero have "moved out" of the grid of considered frequencies, and the numerical solution cannot be trusted any longer.

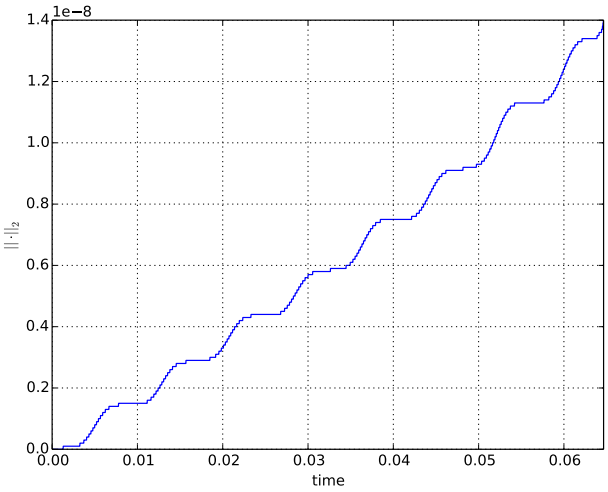

Figure 1. Relative displacement between $\|u(\cdot,t)\|_2^2$ computed along the numerical solution and its initial value $\|u_0\|_2^2$. The numerical experiment considered here is the harmonically trapped multiple re-collision of Section 7.3 with $\gamma_1 = \gamma_2 = 1$, $\gamma_{12} = 10^2$ and $c_1 = c_2 = 0.5$. In this case, by symmetry, $\|u(\cdot,t)\|_2^2 = \|v(\cdot,t)\|_2^2$.

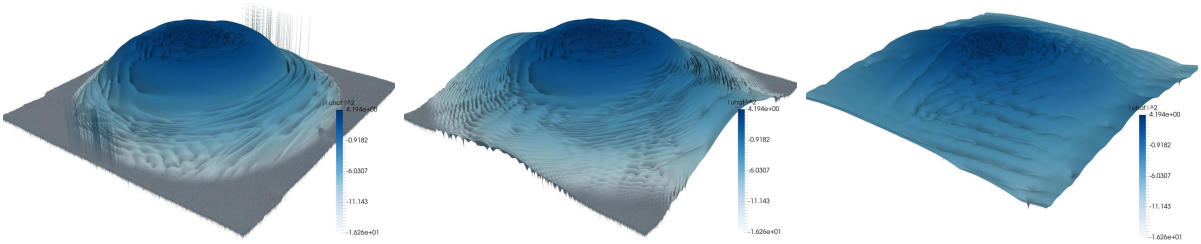

(a) (b) (c)

Figure 2. Plot of $|\widehat{u}(\mathbf{k},t)|$ taken at three consecutive times $t_{(a)} = 0$, $t_{(b)}$, and $t_{(c)}$ during a two-component collision (log-scale in the vertical axis).

As an example, Figure 2 displays a surface plot of $|\widehat{u}(\mathbf{k},t)|$ at times $0 = t_{(a)} < t_{(b)} < t_{(c)}$ for one of the two-component collision experiments performed in Section 7.1. The contribution of the high-frequency modes being several orders of magnitude smaller, a logarithmic scale in the vertical axis is taken for a better visualization. Initially ($t = t_{(a)} = 0$) the plot is perfectly resolved: having chosen the initial datum to be a well-localised Gaussian placed at the centre of the spatial grid (Section 6.4), $|\widehat{u}(\mathbf{k},0)|$ is also a well-localised Gaussian, with all Fourier coefficients of magnitude larger than the machine zero ($\approx 10^{-16}$) fitting well within the $2^{12} \times 2^{12}$ square grid. Later, at $t = t_{(b)}$, when the interaction between the condensates has grown stronger, a considerable amount of high frequency modes are above the machine zero (the vanishing high frequency modes have moved out of the grid), yet remaining below the fidelity threshold of 10^{-6}, which makes us deem this snapshot acceptable. At some further time $t = t_{(c)}$, the interaction between the condensate components develops such a short-scale spatial profile for $u(\mathbf{x},t)$ to resolve which one would need a larger number of Fourier frequencies, whereas in the

Table 1. Parameters used for the initial data of the simulations of one-shot scattering (Section 7.1) and harmonically trapped re-collisions (Section 7.3)

	θ	p_x	p_y	q_x	q_y
u_0	0.05	-100	0	5θ	0
v_0	0.05	100	0	-5θ	0

Table 2. Parameters used for the initial data of the simulations of the component-over-component relaxation (Section 7.2).

	θ	p_x	p_y	q_x	q_y
u_0	0.05	0	0	$\theta/2$	0
v_0	0.05	0	0	$-\theta/2$	0

current resolution the highest frequencies available are of magnitude of 10^0: at this time the simulation can not be trusted.

6.4. Initial data

In all our simulations we choose for each component an initial profile of Gaussian type, namely the (L^2-normalised) wave-function

$$G_{\mathbf{q},\mathbf{p},\theta}(\mathbf{x}) \;:=\; \frac{1}{\theta\sqrt{\pi}}\,\mathrm{e}^{\mathrm{i}\mathbf{p}\cdot\mathbf{x}}\,\exp\left(-\frac{|\mathbf{x}-\mathbf{q}|^2}{2\theta^2}\right) \tag{75}$$

centred at position $\mathbf{q}$ with momentum $\mathbf{p}$ and spread θ.

This is a physically relevant choice, since $G_{\mathbf{q},\mathbf{p},\theta}$ is preparable as the ground state of a suitable harmonic trap, and besides that it can be thought of as the outcome of modern wave-function engineering [19, Section 16.2.4]. Furthermore, this choice is versatile for an amount of numerical simulations: choosing for u_0 and v_0 different $\mathbf{q}$'s and $\mathbf{p}$'s allows one to simulate various kinds of head-on collisions with zero or non-zero impact parameter, taking instead $\mathbf{p} = \mathbf{0}$ and the same $\mathbf{q}$ for both u_0 and v_0 allows one to simulate the relaxation of one component on top of the other, and so on.

Table 1 lists the pool of the initial parameters $(\mathbf{q}, \mathbf{p}, \theta)$ that we considered for the numerical experiments of head-on scattering (Section 7.1) and of multiple re-collisions (Section 7.3) between the two components of the condensate. Table 2 lists the initial parameters for the numerical experiments of component-over-component relaxation (Section 7.2).

We tuned such values so as to guarantee, thanks to a strong enough Gaussian decay of the initial profiles u_0 and v_0, that the initial data are well localised within the spatial domain and in Fourier momentum, and to guarantee also that for all the duration of our numerical experiments the accuracy criteria discussed in Section 6.3 are matched.

Table 3. Parameters for the head-on scattering simulations

n	γ_1	γ_2	γ_{12}	c_1	c_2	$\triangle + 1$	N
1	1	1	10^3	0.50	0.50	$4.00 \cdot 10^{-6}$	2^{12}
2	1	1	10^3	0.40	0.60	$4.17 \cdot 10^{-6}$	2^{12}
3	1	1	10^3	0.10	0.90	$1.11 \cdot 10^{-5}$	2^{12}
4	1	1	10^3	0.01	0.99	$1.01 \cdot 10^{-4}$	2^{12}
5	1	1	$5 \cdot 10^3$	0.01	0.99	$4.04 \cdot 10^{-6}$	2^{14}
6	-1	-1	-200	0.50	0.50	$1.00 \cdot 10^{-4}$	2^{13}
7	-1	-1	-10^3	0.50	0.50	$4.00 \cdot 10^{-6}$	2^{14}
8	10^3	10^3	10^3	0.50	0.50	4	2^{13}
9	10^3	10^3	10^3	0.01	0.99	101	2^{13}
10	-15	-15	-15	0.50	0.50	4	2^{13}
11	10^3	10^3	-10^3	0.50	0.50	4	2^{12}
12	1	1	-200	0.50	0.50	$1 \cdot 10^{-4}$	2^{11}
13	-1	-1	50	0.50	0.50	$1.6 \cdot 10^{-3}$	2^{11}
14	-1	-1	200	0.50	0.50	$1 \cdot 10^{-4}$	2^{11}

7. Numerical analysis: results

In this Section we report and discuss the results of three main groups of numerical experiments.

We test a wide range of possible regimes, which include balanced ($c_1 = c_2$), mildly unbalanced ($c_1 \lesssim c_2$), and strongly unbalanced ($c_1 \ll c_2$) population ratios, as well as intra-species and inter-species interactions ($\alpha \in \{1, 2, 12\}$), of both repulsive ($\gamma_\alpha > 0$) and attractive ($\gamma_\alpha < 0$) type. We also explore various magnitudes of the *miscibility parameter*

$$\triangle \; := \; \frac{\gamma_1 \gamma_2}{c_1 c_2 \gamma_{12}^2} - 1 \tag{76}$$

that discriminates between spatial phase mixing ($\triangle > 0$) or phase separation ($\triangle < 0$) in the ground state associated with our non-linear system (32) [50, Section 21.1], and which determines also the blow-up threshold of the associated initial value problem (as seen explicitly, for example, in the condition (52)).

7.1. One-shot, head-on scattering

The first class of experiments we investigate are one-shot collisions of the two components of a binary condensate initially prepared with a sharp spatial separation and a relative velocity against each other, and left free to scatter away after they have come on top of each other.

Conventionally (see Table 1) we let the scattering process to take place along the x-axis of our spatial grid and we take the u-component to be initially shot from right to

left, the v-component then shot from left to right. Here $U \equiv 0$: each component of the condensate is free to expand ballistically.

For each experiment, labelled with $n = 1, \dots, 14$, we list the corresponding parameters in Table 3. All experiments of this class are performed with resolutions of order $N = 2^{11}$ through $N = 2^{14}$ for each dimension.

We can extract an amount of information from the knowledge of the complex-valued functions $u(\mathbf{x}, t)$ and $v(\mathbf{x}, t)$ of space and time. For example, in Figure 3 we plot for three consecutive times the profile $|u(\mathbf{x}, t)|^2$, which expresses the probability density of particles of the u-component at position $\mathbf{x}$ and time t, together with the phase $\arg u(\mathbf{x}, t)$, whose gradient is proportional to the momentum of the wave-function u. We can detect the collision time and the recoil of the u-component, with a spread in space and momentum.

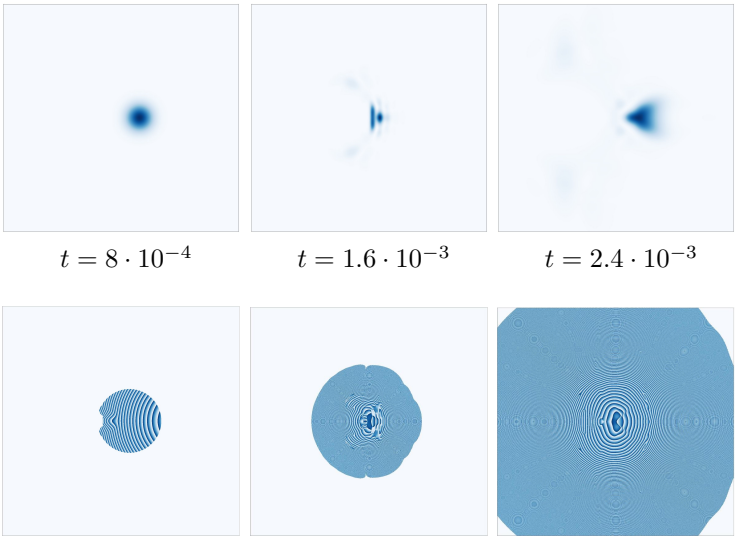

Figure 3. Snapshots of the density profile of $|u(\mathbf{x}, t)|^2$ (top row) and, correspondingly, the phase $\arg u(\mathbf{x}, t)$ (bottom row) at various times during the head-on scattering process between the two components of a binary condensate with interaction parameters $\gamma_1 = \gamma_2 = 1$, $\gamma_{12} = 10^3$ and equal population ratios (experiment $n = 1$ of Table 3). For visualization purposes each snapshot of $|u(\mathbf{x}, t)|^2$ has a different scale, the absolute scale can be inferred from Figure 6.

In a sequence of numerical experiments (cases $n = 1, 2, 3, 4$ of Table 3) we explore the effects of an increasing unbalance in the population ratios on the head-on scattering process with *repulsive* intra-species *and* inter-species interactions, where the two components are initially shot against each other with momenta of equal magnitude and opposite sign. As seen in Section 4.1, this ensures that the system (32) is well posed in H^1 globally in time. In Figure 4 we show that the lower the relative population of the u-component, and hence the lighter the u-condensate, the more its localisation in space is destroyed during the recoil: the density of the u-condensate gets spread in a remarkable pattern around the density of the much more populated (heavier) v-condensate, which

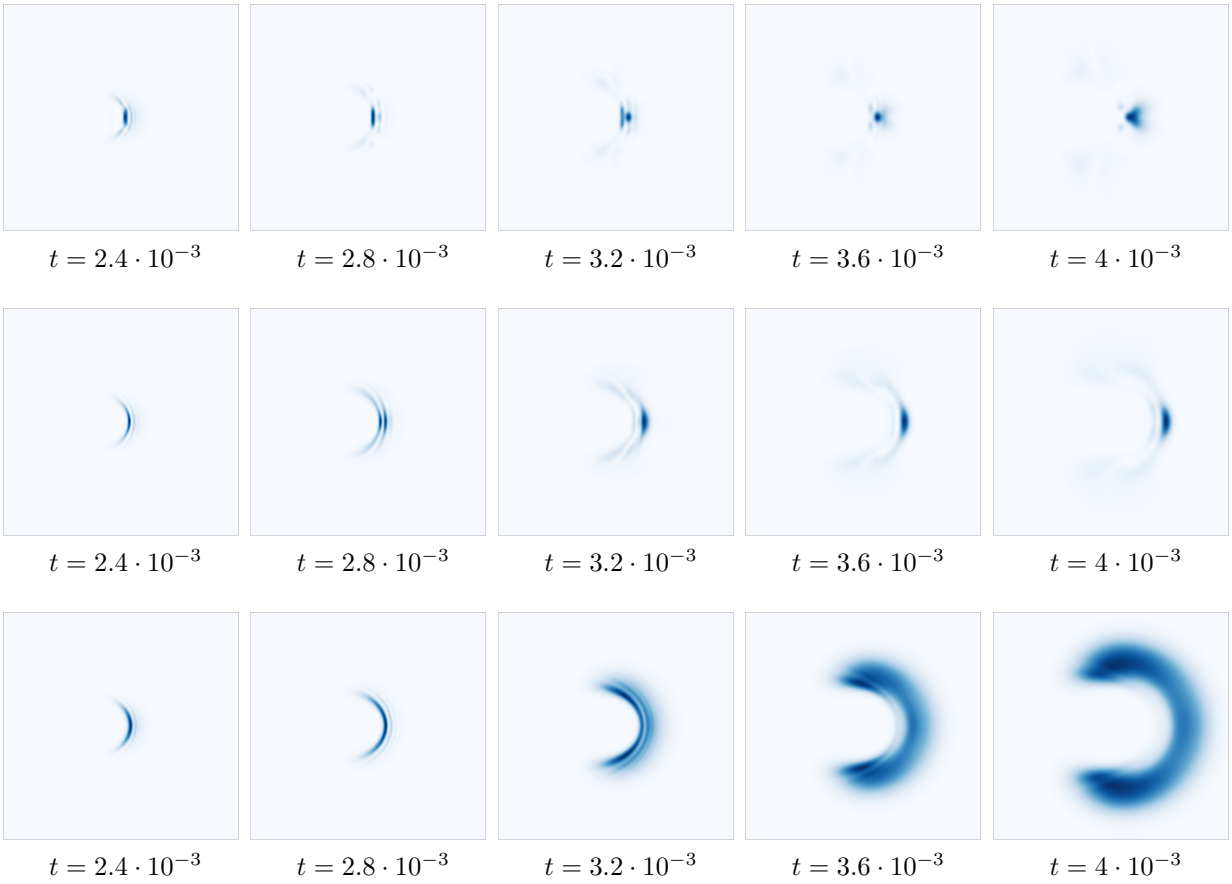

Figure 4. Snapshots of the density profile $|u(\mathbf{x}, t)|^2$ at various times during the head-on scattering process between the two components of a binary condensate. First row: experiment $n = 2$ of Table 3; second row: experiment $n = 3$; third row: experiment $n = 4$. The three experiments have the same interaction parameters $\gamma_1 = \gamma_2 = 1$, $\gamma_{12} = 10^3$ but increasing unbalance in the populations: $c_1 = 0.40, 0.10, 0.01$ from top to bottom. For visualization purposes, along each row the snapshots of $|u(\mathbf{x}, t)|^2$ have a different scale, the absolute scale can be inferred from Figure 6. The numerical evidence is that of a stronger recoil and more drastic delocalisation of the lighter component.

instead remains well localised in space. Figure 5 supplements this picture in terms of the average positions of each components, that is, the vectors

$$\mathbf{X}_u(t) := \int_{\mathbb{R}^2} \mathbf{x}\, |u(\mathbf{x}, t)|^2 \, \mathrm{d}\mathbf{x}\,, \qquad \mathbf{X}_v(t) := \int_{\mathbb{R}^2} \mathbf{x}\, |v(\mathbf{x}, t)|^2 \, \mathrm{d}\mathbf{x}\,. \tag{77}$$

The plot of the horizontal components (x-components) of $\mathbf{X}_u$ and $\mathbf{X}_v$ shows that for balanced or almost balanced populations both components recoil, whereas when the unbalance increases the heavier component preserves its localisation and proceeds along a only slightly changed direction after the collision.

We further investigate head-on collisions with various degree of unbalance in the population ratios (cases $n = 1, 2, 3, 4$ of Table 3) by monitoring the behaviour in time of the norms $\|u(\cdot, t)\|_\infty$ and $\|v(\cdot, t)\|_\infty$. In fact, the profiles of $|u(\mathbf{x}, t)|$ and $|v(\mathbf{x}, t)|$ develop peaks when a concentration of mass occurs, significantly when the two components come

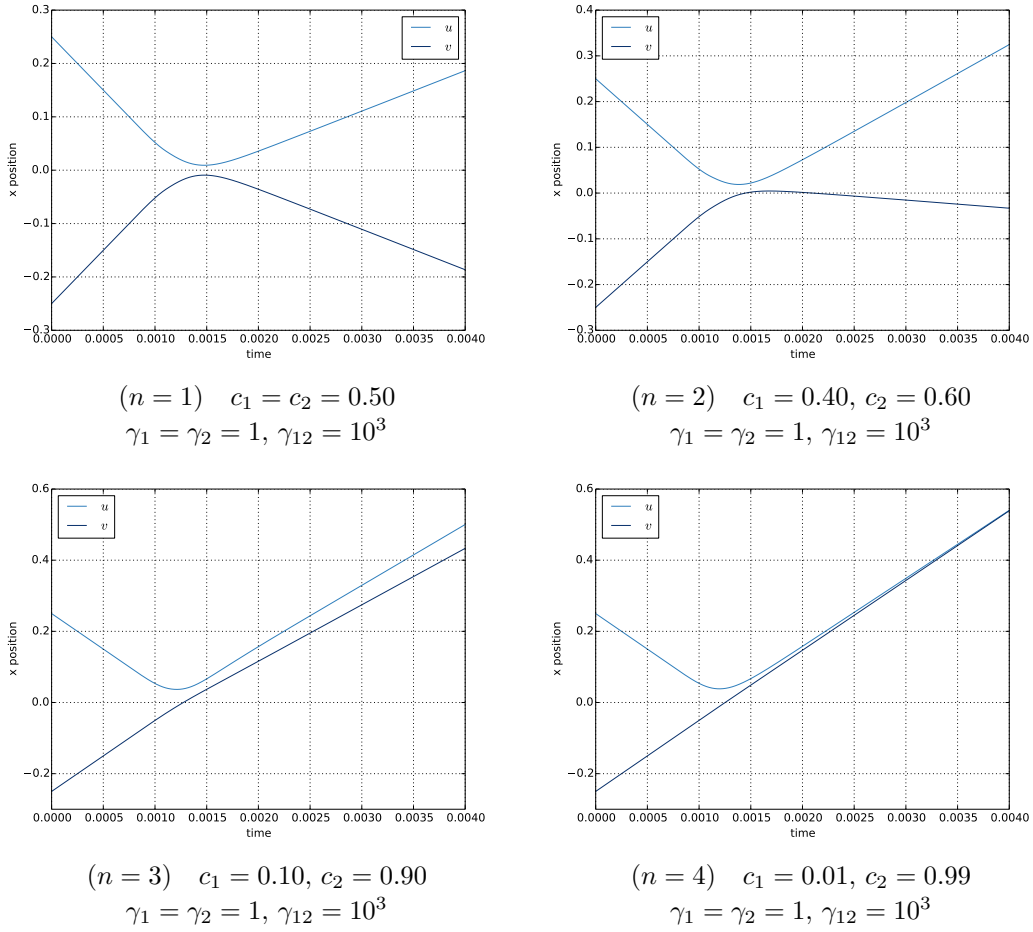

$(n = 1)$ $c_1 = c_2 = 0.50$
$\gamma_1 = \gamma_2 = 1$, $\gamma_{12} = 10^3$

$(n = 2)$ $c_1 = 0.40$, $c_2 = 0.60$
$\gamma_1 = \gamma_2 = 1$, $\gamma_{12} = 10^3$

$(n = 3)$ $c_1 = 0.10$, $c_2 = 0.90$
$\gamma_1 = \gamma_2 = 1$, $\gamma_{12} = 10^3$

$(n = 4)$ $c_1 = 0.01$, $c_2 = 0.99$
$\gamma_1 = \gamma_2 = 1$, $\gamma_{12} = 10^3$

Figure 5. Time behaviour of the average positions $\mathbf{X}_u(t)$ and $\mathbf{X}_v(t)$ (along the x-axis of the spatial grid) of each component of a binary condensate during the head-on scattering process between components, relative to the numerical experiments $n = 1, 2, 3, 4$ from Table 3. An effect emerges of the population unbalance.

spatially on top of each other: the L^∞-norm captures the appearance of such peaks. In Figure 6 we show that sufficiently far in time before or after the actual collision phase the L^∞-norm of each component decreases with a typical dispersive behaviour, and this happens for any population ratio. During the collision phase, instead, the L^∞-norm undergoes a rapid increase, followed by a somewhat less rapid decrease. Moreover, the lighter a component, the more pronounced is the jump of its L^∞-norm.

Last, as far as the strong population unbalance is concerned, we find it instructive to study the difference, in the scattering between heavy and a light component, between two opposite cases in which the inter-species repulsion is greatly larger than or comparable to the intra-species repulsion, respectively, experiment $n = 5$ and $n = 9$ from Table 3. Figure 7 shows our numerical evidence. In the former case, as commented above, the localisation of the light component is destroyed and its profile is spread backwards. In the latter, instead, the light component recoils slowly with a mild spread and a definite

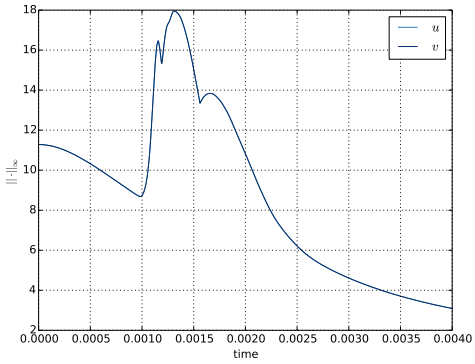

$(n = 1) \quad c_1 = c_2 = 0.50$
$\gamma_1 = \gamma_2 = 1,\ \gamma_{12} = 10^3$

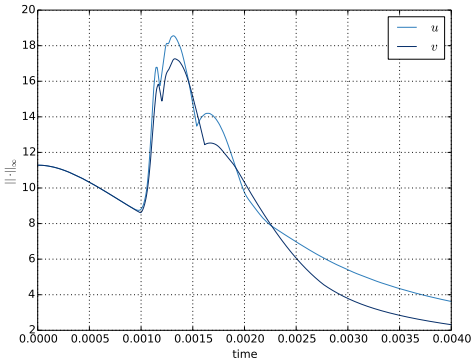

$(n = 2) \quad c_1 = 0.40,\ c_2 = 0.60$
$\gamma_1 = \gamma_2 = 1,\ \gamma_{12} = 10^3$

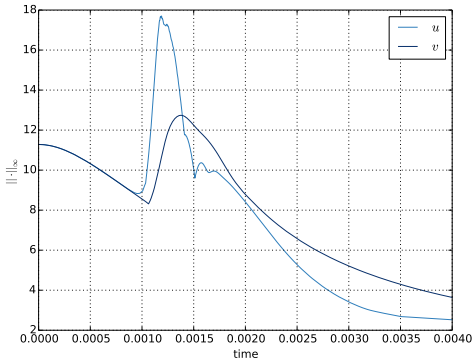

$(n = 3) \quad c_1 = 0.10,\ c_2 = 0.90$
$\gamma_1 = \gamma_2 = 1,\ \gamma_{12} = 10^3$

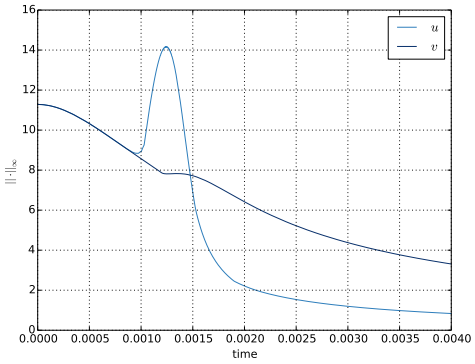

$(n = 4) \quad c_1 = 0.01,\ c_2 = 0.99$
$\gamma_1 = \gamma_2 = 1,\ \gamma_{12} = 10^3$

Figure 6. Time behaviour of the norms $\|u(\cdot,t)\|_\infty$ and $\|v(\cdot,t)\|_\infty$ during the head-on scattering process between the two components of a binary condensate, relative to the numerical experiments $n = 1$ and $n = 2$ (top row) and $n = 3$ and $n = 4$ (bottom row) from Table 3. An effect emerges of the population unbalance, as discussed Section 7.1.

localisation; moreover, in the short period of spatial overlap between components the inter-species repulsion acts most effectively where the density profile is more pronounced, namely in the region of the peak. This results in a typical 'crater' excavated in the profile of the light component, which is then preserved in the subsequent recoil.

We then turn to explore the effects of different magnitudes of the intra- and inter-species interactions when the collision takes place between component of equal populations. Two paradigmatic patterns emerge. When an *attraction* between the two components is present, of significantly stronger magnitude than the intra-species coupling (be the latter positive or negative), a characteristic 'squeezing-and-shooting' effect occurs in which the two profiles undergo a very quick and pronounced contraction in the region of spatial overlap, followed by the ejection of two very much focused and elongated wave packets in opposite directions (numerical experiments $n = 12$ and $n = 7$ in the first two rows of Figure 8). Instead, when between the two components a *repulsion* is

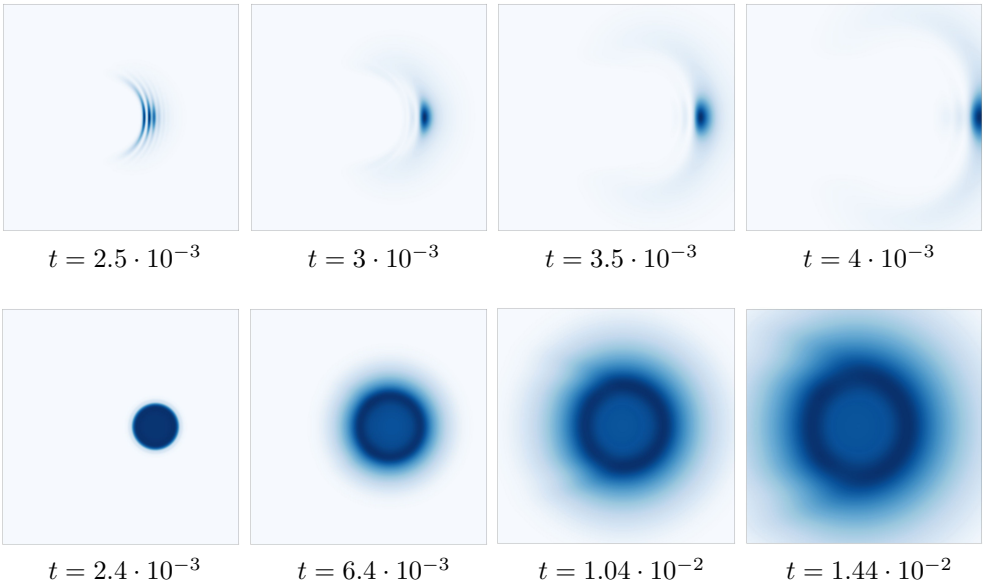

Figure 7. Snapshots of the density profile $|u(\mathbf{x}, t)|^2$ of the light component at various times during the head-on scattering process between the two components of a binary condensate. Top row: experiment $n = 5$ of Table 3 ($\gamma_1 = \gamma_2 = 1$, $\gamma_{12} = 5 \cdot 10^3$, $c_1 = 0.01$); bottom row: experiment $n = 9$ ($\gamma_1 = \gamma_2 = \gamma_{12} = 10^3$, $c_1 = 0.01$). For visualization purposes, along each row the snapshots of $|u(\mathbf{x}, t)|^2$ have a different scale, the absolute scale can be inferred from Figure 6.

present of much stronger magnitude than the inter-species coupling, this results in a 'splash-the-blob' effect caused by the violent expansion of the two profiles under the the strong repulsion occurring at the moment of their spatial overlap, thus followed by a wide spread of each cloud and possibly by the production of two distinct upper and lower sub-clouds with respect of the incident direction (numerical experiments $n = 13$ and $n = 14$ in the last two rows of Figure 8).

Additional information is provided by the time behaviour of the L^∞-norm of each profile, as displayed in Figure 9. The two opposite patterns are a blow-up in short time, as opposite to a typical dispersive behaviour with gradual decrease in time of the L^∞-norm of each profile. The former can be driven by an ultra-strong inter-species attraction (numerical experiment $n = 7$) *or also* by the simultaneous presence of attractive interactions inside each component and between the two components, as long as the magnitude of such interactions is comparable (numerical experiments $n = 10$). The latter, namely a gradual decrease of the L^∞-norm of dispersive type, occurs in the presence of repulsive interactions (the 'splash' phenomenon of experiments $n = 13, 14$) or also when the inter-species repulsion has a considerably stronger, but not critically strong, magnitude than the intra-species interaction (the 'squeezing and shooting' phenomenon of experiments $n = 6, 12$): in either case a quick formation of a (mild) peak in the L^∞-norm reveals distinctly the phase in which the two profiles overlap and interact strongly, before coming apart.

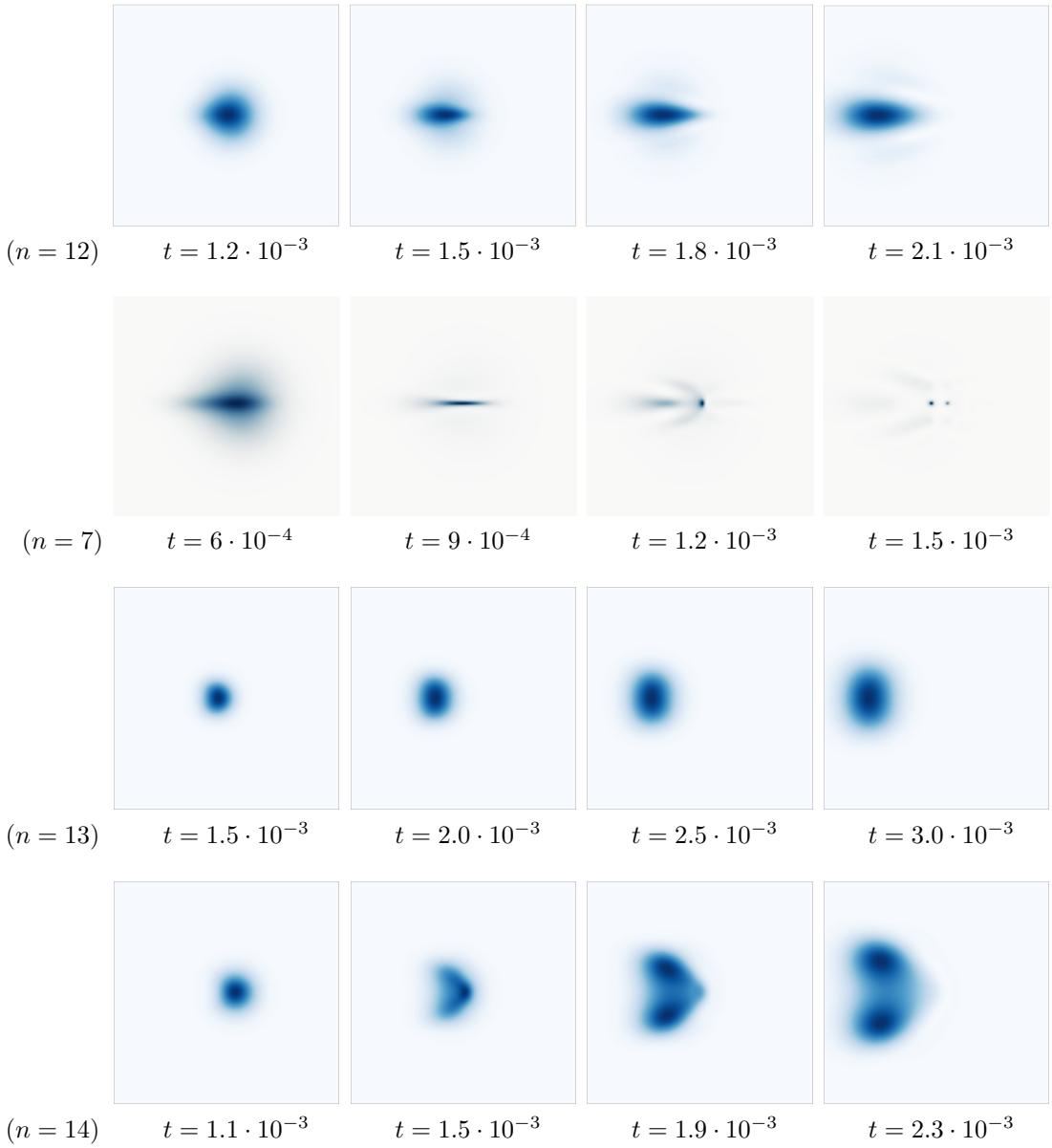

Figure 8. Snapshots of the density profile $|u(\mathbf{x}, t)|^2$ at various times during the head-on scattering process between the two equally populated components of a binary condensate. 'Squeezing-and-shooting' effect in the first two rows, corresponding respectively to experiments $n = 12$ ($\gamma_1 = \gamma_2 = 1$, $\gamma_{12} = -200$) and $n = 7$ ($\gamma_1 = \gamma_2 = -1$, $\gamma_{12} = -10^3$) of Table 3. 'Splash-the-blob' effect in the last two rows, corresponding respectively to experiments $n = 13$ ($\gamma_1 = \gamma_2 = -1$, $\gamma_{12} = 50$), and $n = 14$ ($\gamma_1 = \gamma_2 = -1$, $\gamma_{12} = 200$) of Table 3. For visualization purposes, along each row the snapshots of $|u(\mathbf{x}, t)|^2$ have a different scale, the absolute scale can be inferred from Figure 9. Discussion in Section 7.1.

7.2. Condensate-over-condensate relaxation

The second class of experiments we investigate are the relaxations of one component over the other in a binary condensate with both populations initially localised in the

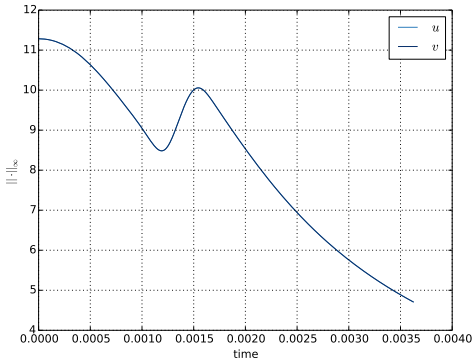

$(n = 6)$ $c_1 = c_2 = 0.5$
$\gamma_1 = \gamma_2 = -1$, $\gamma_{12} = -200$

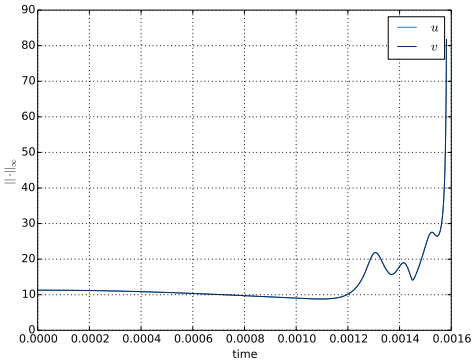

$(n = 7)$ $c_1 = c_2 = 0.5$
$\gamma_1 = \gamma_2 = -1$, $\gamma_{12} = -10^3$

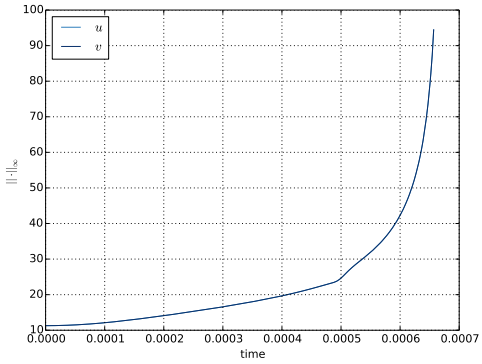

$(n = 10)$ $c_1 = c_2 = 0.5$
$\gamma_1 = \gamma_2 = \gamma_{12} = -15$

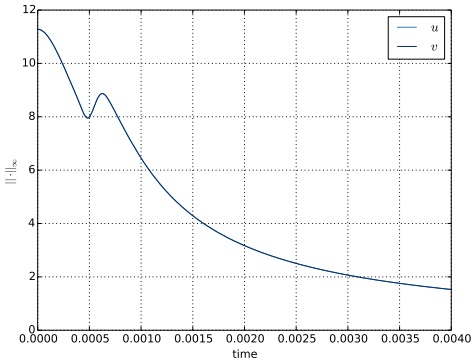

$(n = 12)$ $c_1 = c_2 = 0.5$
$\gamma_1 = \gamma_2 = 1$, $\gamma_{12} = -200$

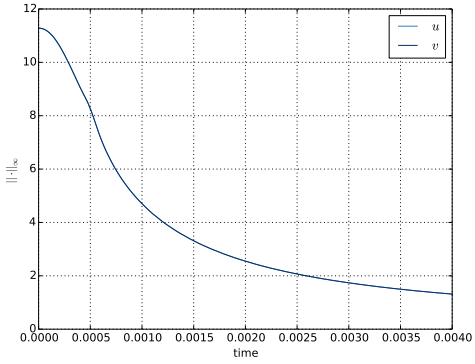

$(n = 13)$ $c_1 = c_2 = 0.5$
$\gamma_1 = \gamma_2 = 1$, $\gamma_{12} = 50$

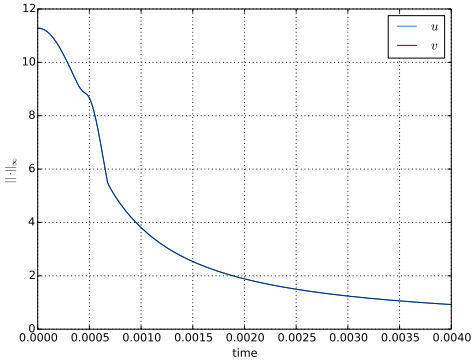

$(n = 14)$ $c_1 = c_2 = 0.5$
$\gamma_1 = \gamma_2 = 1$, $\gamma_{12} = 200$

Figure 9. Time behaviour of $\|u(\cdot,t)\|_\infty$ during the head-on scattering process between the two equally populated components of a binary condensate, relative to numerical experiments $n = 6, 7, 10, 12, 13, 14$ from Table 3. By symmetry $\|v(\cdot,t)\|_\infty$ has the same plot.

same region. Also in this case we take $U \equiv 0$, that is, the relaxation is not trapped.

In order to magnify the relevant features of the dynamics, we introduce a small

Table 4. Parameters for the relaxation simulations

n	γ_1	γ_2	γ_{12}	c_1	c_2	$\triangle + 1$	N_0
15	1	1	10^3	0.50	0.50	$4 \cdot 10^{-6}$	2^{10}
16	1	1	10^3	0.40	0.60	$4.17 \cdot 10^{-6}$	2^{11}
17	1	1	10^3	0.10	0.90	$1.1 \cdot 10^{-5}$	2^{11}
18	1	1	10^3	0.01	0.99	10^{-4}	2^{11}
19	1	1	10^4	0.01	0.99	10^{-6}	2^{12}
20	-10^3	-10^3	-10^3	0.50	0.50	4	2^{12}
21	-10^3	-10^3	-10^3	0.01	0.99	101	2^{12}
22	-20	-20	20	0.50	0.50	4	2^{11}
23	-1	-1	200	0.50	0.50	$1 \cdot 10^{-4}$	2^{11}

displacement between the centres of the Gaussian profiles of the initial data, with the u-component (resp., the v-component) slightly shifted to the right (resp., to the left) along the x-axis. Each profile has zero momentum at the beginning. The precise initial conditions are summarised in Table 2.

Several competing effects enter the relaxation process: the dispersive nature of the kinetic operator in the system (32) favours a gradual spread in space of the solutions, repulsive interactions (de-focusing couplings) enhance further this effect whereas attractive interactions (focusing couplings) tend to contrast it, and the relative balance between intra-species and inter-species interactions, encoded in the parameter $\triangle$ defined in (76) further pushes towards reinforcing or suppressing the expansion of the two clouds.

In a first round of experiments (cases $n = 15, 16, 17, 18, 19$ of Table 4) we explore the effects of an increasing unbalance in the population ratios on the relaxation process, in the presence of repulsive interactions among particles of any type, and where the inter-species repulsion has a much stronger magnitude than the intra-species one. For the first four cases, the time step we use is $h = 10^{-6}$, whereas for the fifth case we use $h = 2 \cdot 10^{-7}$.

In Figure 10 we show that when the two components are (almost) equally populated the corresponding profiles separate and disperse gradually in time, with an asymmetric spatial distribution that reflects the asymmetry of the configuration at time $t = 0$: thus, the u-component goes shifted away to the right, and the v-component to the left. The more the population ratios become unbalanced, the slower and more symmetrically the profile of the heavy component spreads, pushing away the light component around it. In this regime, the strong unbalance between heavy and light component overcomes relatively soon the spatial asymmetry of the initial configuration: the two clouds expand radially, the heavier one well localised around the initial position, the lighter one pushed away in an annulus around the heavier with several circular waves following the main wave, which become more packed as γ_{12} increases.

Correspondingly, no dramatic concentration of mass occurs in the relaxation process,

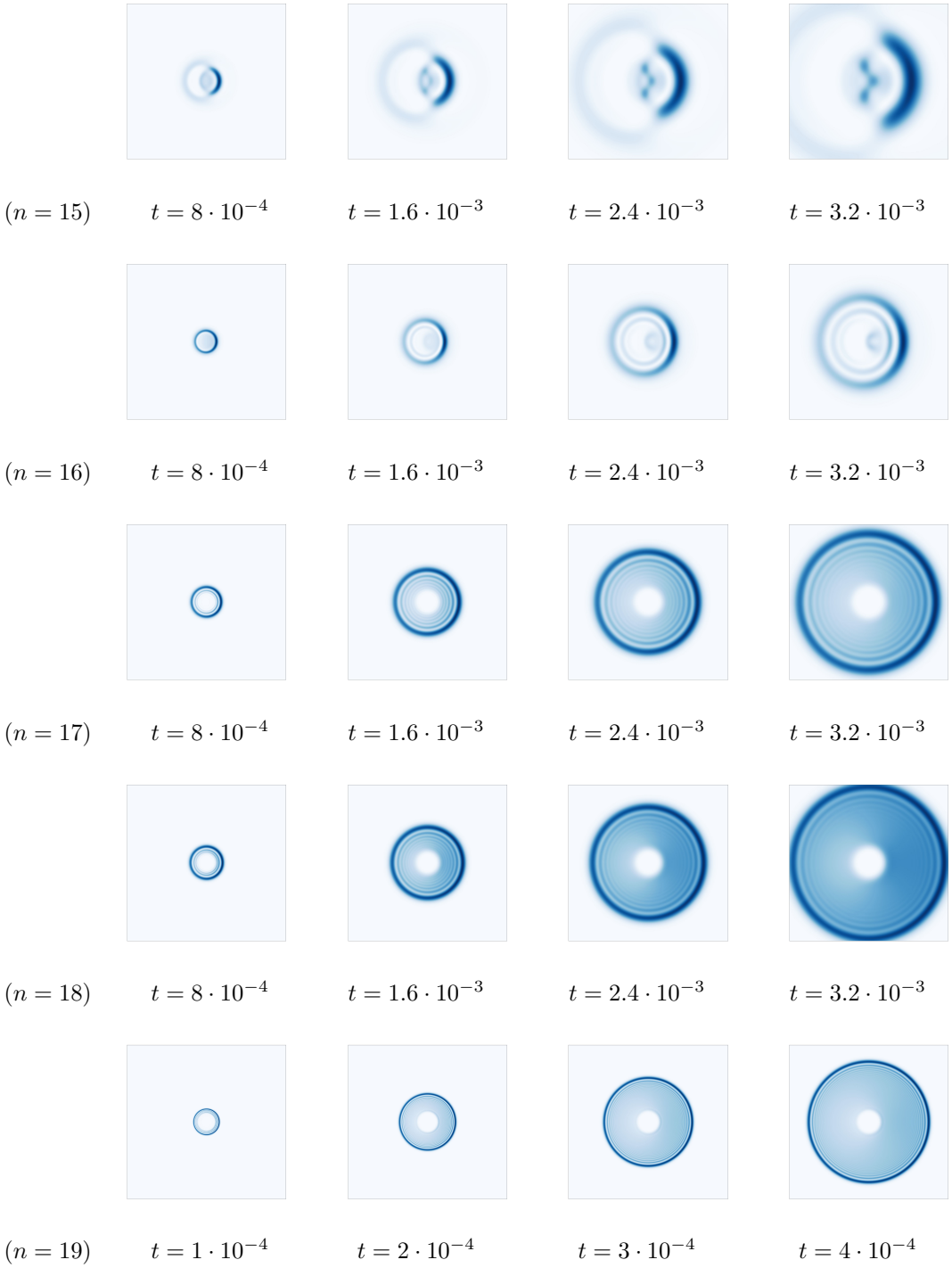

Figure 10. Snapshots of the density profile $|u(\mathbf{x}, t)|^2$ of the light component at various times during the relaxation of a binary condensates (both components on top of each other). First four rows: interaction couplings $\gamma_1 = \gamma_2 = 1$, $\gamma_{12} = 10^3$) and increasing unbalance in the populations, $c_1 = 0.50, 0.40, 0.10, 0.01$ from top to bottom. Last row: $c_1 = 0.01$, $c_2 = 0.99$, $\gamma_1 = \gamma_2 = 1$, $\gamma_{12} = 10^4$. These are the numerical experiments $n = 15, 16, 17, 18, 19$ of Table 4. For visualization purposes, along each row the snapshots have a different scale, the absolute scale can be inferred from Figure 11.

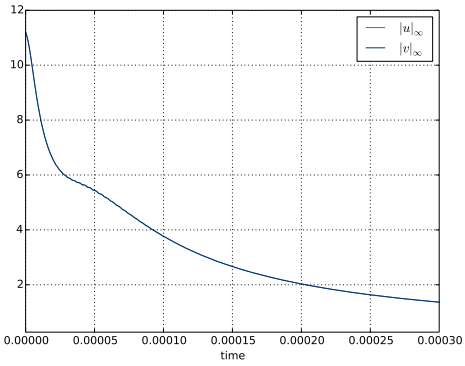

$(n = 15)$ $c_1 = 0.50$, $c_2 = 0.50$
$\gamma_1 = \gamma_2 = 1$, $\gamma_{12} = 10^3$

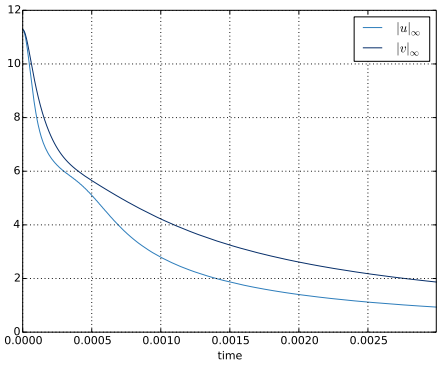

$(n = 16)$ $c_1 = 0.40$, $c_2 = 0.60$
$\gamma_1 = \gamma_2 = 1$, $\gamma_{12} = 10^3$

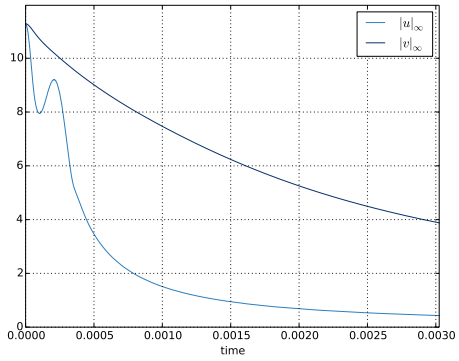

$(n = 17)$ $c_1 = 0.10$, $c_2 = 0.90$
$\gamma_1 = \gamma_2 = 1$, $\gamma_{12} = 10^3$

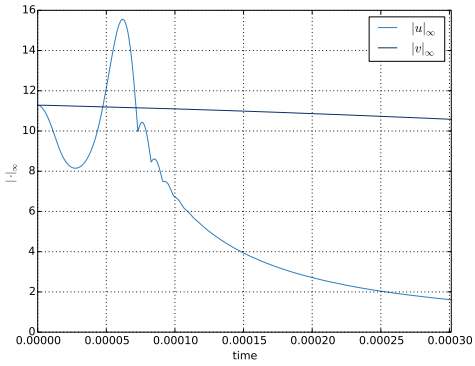

$(n = 19)$ $c_1 = 0.01$, $c_2 = 0.99$
$\gamma_1 = \gamma_2 = 1$, $\gamma_{12} = 10^4$

Figure 11. Time behaviour of the norms $\|u(\cdot,t)\|_\infty$ and $\|v(\cdot,t)\|_\infty$ during the component-over-component relaxation of a binary condensate relative to the numerical experiments $n = 15, 16, 17, 19$ of Table 4.

as our control of the L^∞-norms of the two profiles reveals (Figure 11). Only when one component is extremely lighter (less populated), does its profile undergo the quick formation of an annular peak of considerable magnitude, around the profile of the heavy component, before the dispersive effects take over. Such a violent increase of the L^∞-norm of the ultra-light profile persists only for short time and must not be confused with a proper blow-up, which in fact in this regime cannot occur (Section 4.1).

All this provides a novel and more structured evidence of the dynamical formation of phase separation in the non-miscibility regime $\triangle < 0$ for a binary condensate, an experimental feature [20, 19] that has been partially reproduced by recent numerical studies [15, 27].

We further analyze the relaxation process through the behaviour in time of the average positions $\mathbf{X}_u(t)$ and $\mathbf{X}_v(t)$ of each component (see definition (77)), both under a change in the interactions and in the population ratios. With Figure 12 we find a further sharp evidence that in the repulsive regime, the lighter one component, the faster it gets

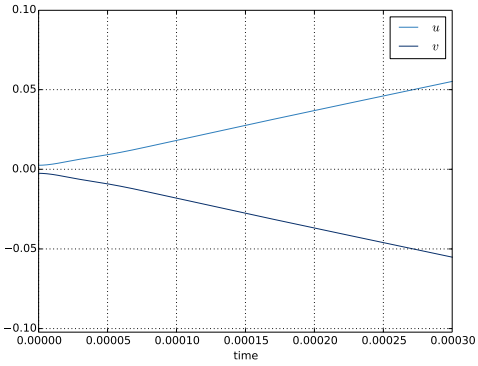

$(n = 15)$ $c_1 = 0.50$, $c_2 = 0.50$
$\gamma_1 = \gamma_2 = 1\,,\quad \gamma_{12} = 10^3$

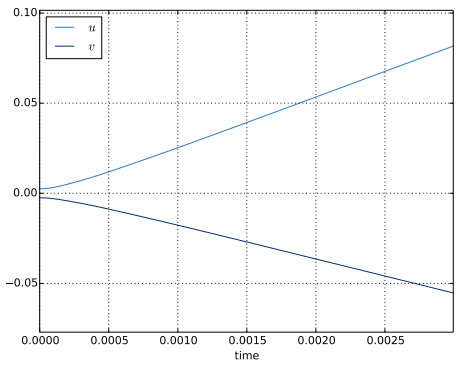

$(n = 16)$ $c_1 = 0.40$, $c_2 = 0.60$
$\gamma_1 = \gamma_2 = 1\,,\quad \gamma_{12} = 10^3$

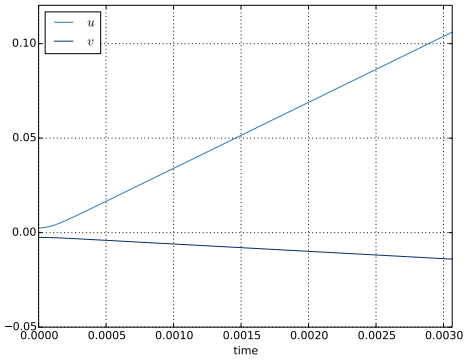

$(n = 17)$ $c_1 = 0.10$, $c_2 = 0.90$
$\gamma_1 = \gamma_2 = 1\,,\quad \gamma_{12} = 10^3$

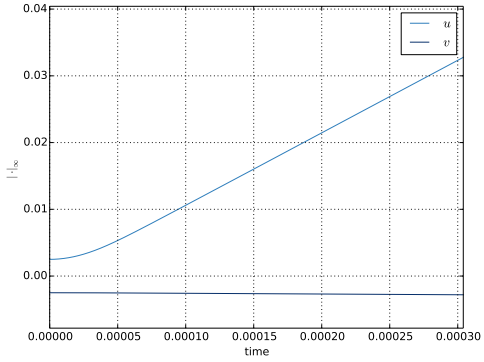

$(n = 19)$ $c_1 = 0.01$, $c_2 = 0.99$
$\gamma_1 = \gamma_2 = 1\,,\quad \gamma_{12} = 10^4$

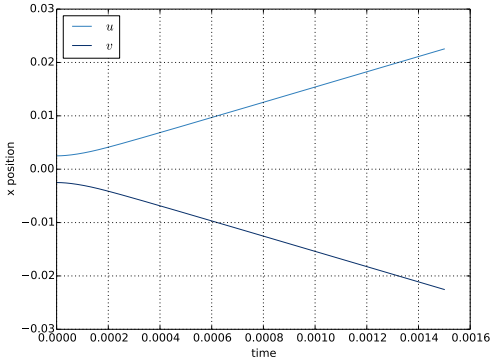

$(n = 20)$ $c_1 = 0.50$, $c_2 = 0.50$
$\gamma_1 = \gamma_2 = \gamma_{12} = -10^3$

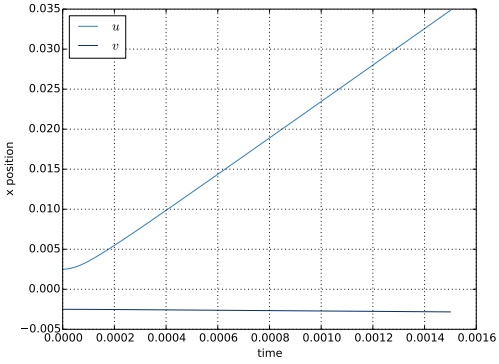

$(n = 21)$ $c_1 = 0.01$, $c_2 = 0.99$
$\gamma_1 = \gamma_2 = \gamma_{12} = -10^3$

Figure 12. Time behaviour of the average positions $\mathbf{X}_u(t)$ and $\mathbf{X}_v(t)$ (along the x-axis of the spatial grid) of each component of a binary condensate during the component-over-component relaxation, experiments $n = 15, 16, 17, 19, 20, 21$ of Table 4.

pushed away from the heavy one, which remains instead almost steady, whereas when the population ratios are comparable the two component profiles get far apart almost symmetrically. Remarkably, when instead intra-species and inter-species interactions are

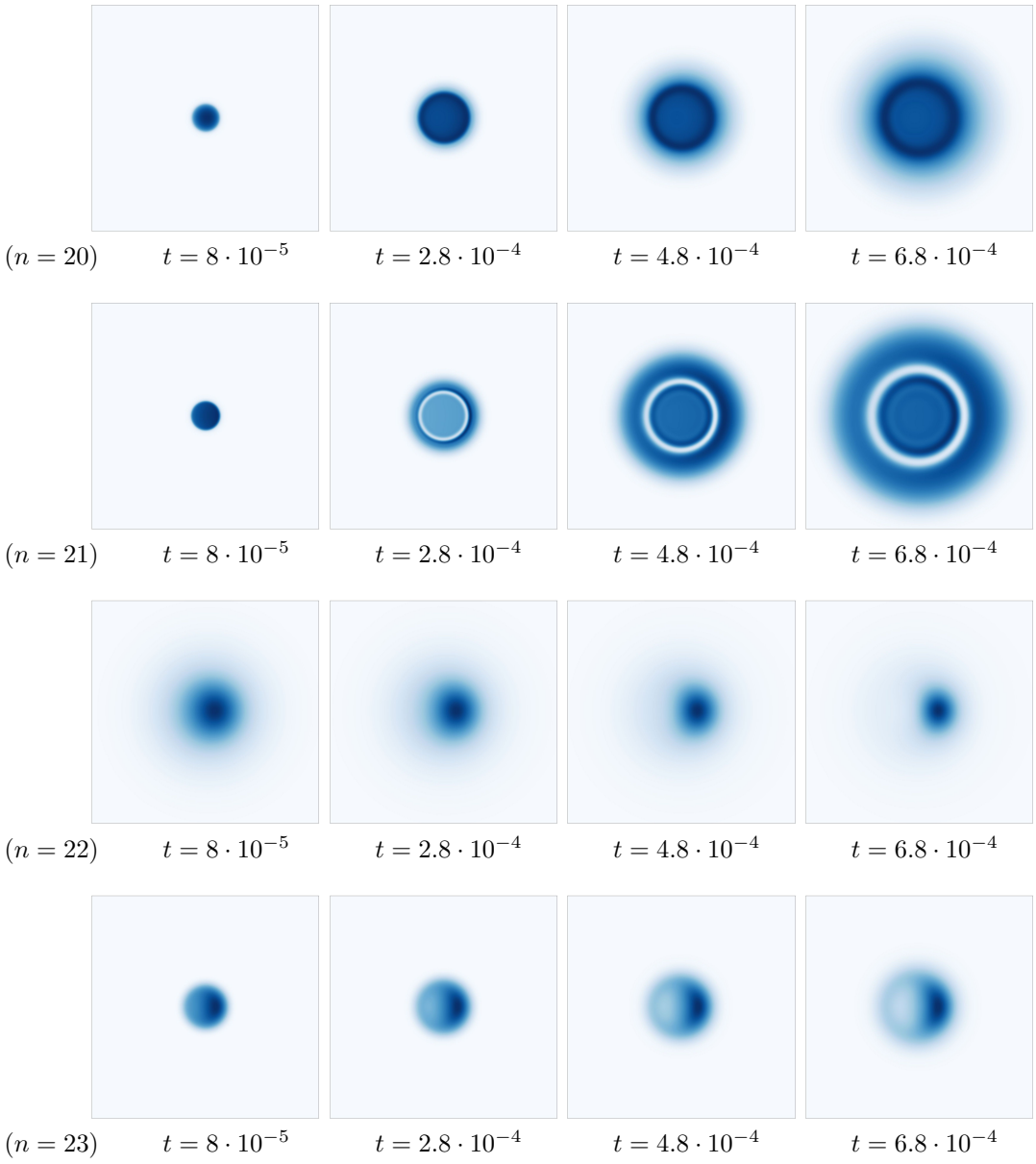

Figure 13. Snapshots of the density profile $|u(\mathbf{x}, t)|^2$ of the light component at various times during the relaxation of a binary condensates (components on top of each other). First row: numerical experiment $n = 20$ of Table 4 ($c_1 = c_2 = 0.5$, $\gamma_1 = \gamma_2 = \gamma_{12} = -10^3$). Second row: experiment $n = 21$ ($c_1 = 0.1$, $\gamma_1 = \gamma_2 = \gamma_{12} = -10^3$). Third row: experiment $n = 22$ ($c_1 = c_2 = 0.5$, $\gamma_1 = \gamma_2 = -20$ and $\gamma_{12} = 20$). Fourth row: experiment $n = 23$ ($c_1 = c_2 = 0.5$, $\gamma_1 = \gamma_2 = -1$, $\gamma_{12} = 200$). For visualization purposes, along each row the snapshots have a different scale: for example, the absolute scale for the cases $n = 8, 9$ can be inferred from Figure 14.

turned to attractive and with comparable magnitude (numerical experiments $n = 20, 21$ of Table 4), this results in an appreciable competing effect against the dispersion induced by the linear part of the dynamics and in a much slower speed separation. For example, comparing the cases $n = 15$ and $n = 20$ in Figure 12, both with equal populations, it

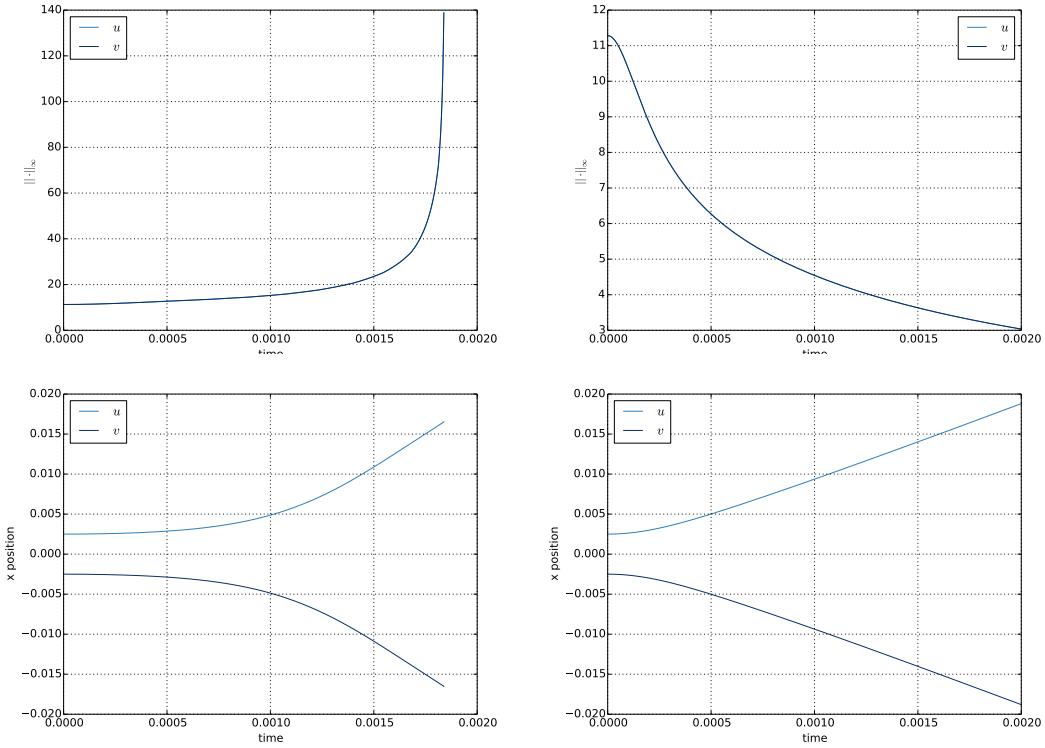

$(n = 22) \quad c_1 = c_2$
$\gamma_1 = \gamma_2 = -20,\ \gamma_{12} = 20$

$(n = 23) \quad c_1 = c_2$
$\gamma_1 = \gamma_2 = -1,\ \gamma_{12} = 200$

Figure 14. Time behaviour of the norm $\|u(\cdot,t)\|_\infty$ and of the average positions $\mathbf{X}_u(t)$ and $\mathbf{X}_v(t)$ (along the x-axis of the spatial grid) of each component of a binary condensate during the component-over-component relaxation, relative to experiments $n = 22$ (left column) and $n = 23$ (right column) of Table 4. By symmetry $\|v(\cdot,t)\|_\infty = \|u(\cdot,t)\|_\infty$.

takes a 10 times longer period in the second case (competing attraction, slow separation) for $|\mathbf{X}_u(t) - \mathbf{X}_v(t)|$ to attain the same value as in the first case (repulsion and hence fast separation). In the repulsive regime too we observe the same asymmetric escape of the light component in case of strong unbalance among populations (compare, for instance, the cases $n = 16$ and $n = 21$ in Figure 12).

In the round of numerical experiments displayed in Figure 13 (cases $n = 20, 21, 22, 23$ of Table 4) we supplement the picture above also in new regimes. First, we detect the same mechanism of 'crater' formation, already encountered in the collision scenario, also in the presence of attractive interactions, which is more pronounced in the profile of the ultra-light component ($n = 20, 21$). Concerning the mixed repulsion/attraction effects, we then observe a relaxation in which the phase separation is initially driven by a repulsion between components, until when each component collapses under the effect of an intra-species attraction ($n = 22$). When, instead, the inter-species repulsion is so strong to overcome the intra-species attraction, then the relaxation proceeds in time with a more and more definite spatial separation ($n = 23$).

We find additional information on the last two cases of relaxation under the

Table 5. Parameters for the harmonically trapped re-collision simulations.

n	γ_1	γ_2	γ_{12}	c_1	c_2	$\triangle + 1$	N_0
24	1	1	10^3	0.50	0.50	$4 \cdot 10^{-6}$	2^{13}
25	1	1	10^3	0.10	0.90	$1.1 \cdot 10^{-5}$	2^{13}
26	1	1	10^3	0.01	0.99	10^{-6}	2^{13}
27	1	1	$5 \cdot 10^3$	0.50	0.50	$1.6 \cdot 10^{-7}$	2^{13}
28	1	1	-200	0.50	0.50	$1 \cdot 10^{-4}$	2^{12}
29	-1	-1	50	0.50	0.50	$1.6 \cdot 10^{-3}$	2^{11}

competing effect of attraction inside each component and repulsion among components, by comparing in Figure 14 the time behaviour of the norms $\|u(\cdot,t)\|_\infty$ and $\|v(\cdot,t)\|_\infty$, and of the average positions $\mathbf{X}_u(t)$ and $\mathbf{X}_v(t)$. In particular, depending on the relative magnitude between attraction and repulsion, the component separation may come with a collapse in each component, each profile spiking up to a delta-like shape and its L^∞-norm diverging.

7.3. Multiple re-collisions for a harmonically trapped binary condensate

As a third class of simulations, we consider the component-component multiple re-collisions occurring in a harmonically trapped binary condensate.

The initial data, with parameters listed in Table 1, are the same as those used for the single-collision simulations (Section 7.1), that is, two components shot against each other. The system (32) is now solved with the harmonic potential (41), namely

$$U(\mathbf{x}) \;=\; \omega^2|\mathbf{x}|^2\,, \qquad \omega = 10^2\,, \tag{78}$$

where the constant ω is chosen by trial and error so that in all the considered experiments the solution profiles remain well localised within the computational grid and the simulations can be resolved numerically. To this aim, we also enlarge the computational domain to $[-2\pi, 2\pi] \times [-2\pi, 2\pi]$. Table 5 lists the interaction parameters and population ratios for the numerical experiments of this series. We chose them essentially by selecting those relevant cases from the single-collision scenario for which our numerics provides the cleanest evidence.

Owing to the harmonic confinement, the two components undergo a pulsing behaviour typically consisting of re-collisions followed by escapes towards opposite directions. In order to compute several of such events, a considerably longer time integration is required, to achieve which with acceptable accuracy we *reduce the time step* to $h = 2 \cdot 10^{-7}$. With this choice, the relative mass loss exceeds the fidelity threshold of 10^{-5} (our criterion (74)) in approximately $4 \cdot 10^5$ time steps.

Analogously to the single collision case (Section 7.1) in the presence of repulsive interactions, we find that the solutions exhibit a repeated recoil pattern when the two components are equally populated, whereas when a considerably heavier component

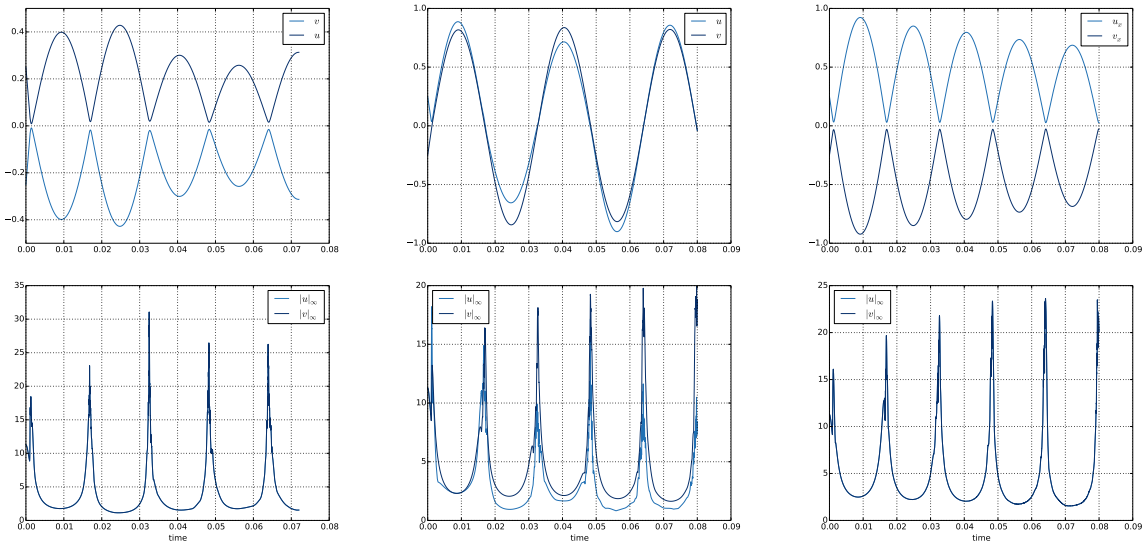

$(n=24)$ $\begin{matrix} c_1=0.5 \\ c_2=0.5 \end{matrix}$, $\begin{matrix} \gamma_{12}=10^3 \\ \gamma_1=\gamma_2=1 \end{matrix}$ $(n=25)$ $\begin{matrix} c_1=0.1 \\ c_2=0.9 \end{matrix}$, $\begin{matrix} \gamma_{12}=10^3 \\ \gamma_1=\gamma_2=1 \end{matrix}$ $(n=27)$ $\begin{matrix} c_1=0.5 \\ c_2=0.5 \end{matrix}$, $\begin{matrix} \gamma_{12}=5\cdot 10^3 \\ \gamma_1=\gamma_2=1 \end{matrix}$

Figure 15. Time behaviour of the norms $\|u(\cdot,t)\|_\infty$ and $\|v(\cdot,t)\|_\infty$ (top row) and of the average positions $\mathbf{X}_u(t)$ and $\mathbf{X}_v(t)$ along the x-axis of the spatial grid (bottom row) of each component of a binary condensate during the harmonically trapped multiple re-collision process with various interaction parameters and population ratios (from left to right: experiment $n=24,25,27$ of Table 5)

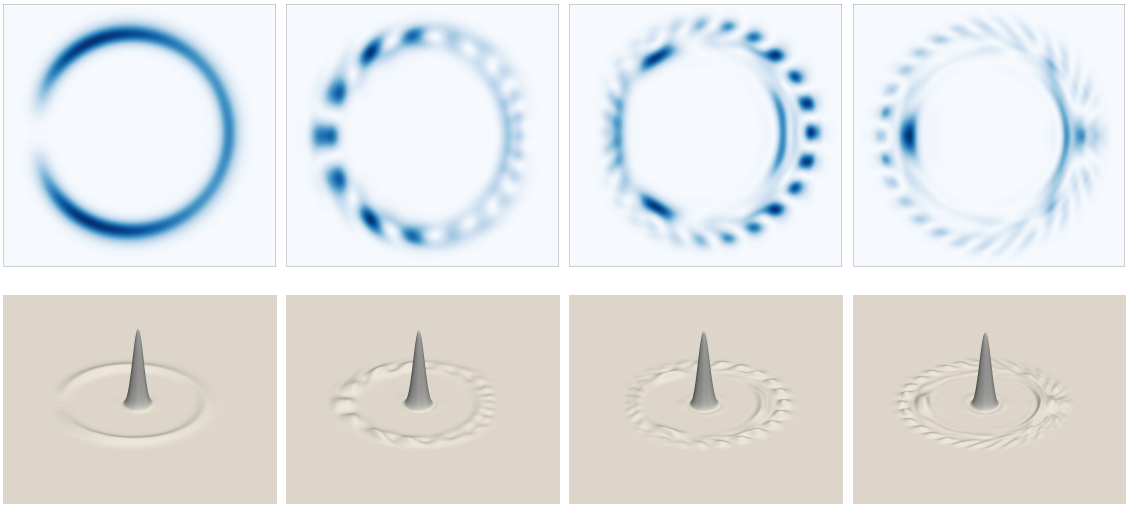

$t=9.2\cdot 10^{-3}$ $t=2.48\cdot 10^{-2}$ $t=4.04\cdot 10^{-2}$ $t=5.6\cdot 10^{-2}$

Figure 16. Snapshots of the density profile $|u(\mathbf{x},t)|^2$ of the light component (top row) and of both profiles $|u(\mathbf{x},t)|^2$ and $|v(\mathbf{x},t)|^2$ (bottom row) at various times during the harmonically trapped re-collisions of the components of a binary condensate with interaction parameters $\gamma_1=\gamma_2=1$, $\gamma_{12}=10^3$ and population ratios $c_1=0.01$, $c_2=0.99$ (experiment $n=26$ of Table 5). The snapshots are taken after consecutive re-collisions at the instants of velocity inversion.

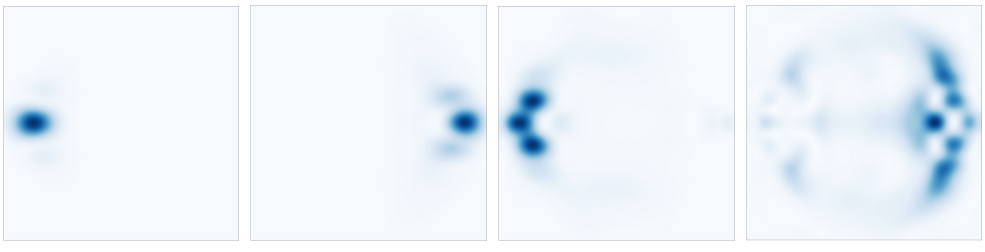

$(n = 28)$ $t = 8.8 \cdot 10^{-3}$ $t = 2.48 \cdot 10^{-2}$ $t = 4.06 \cdot 10^{-2}$ $t = 5.66 \cdot 10^{-2}$

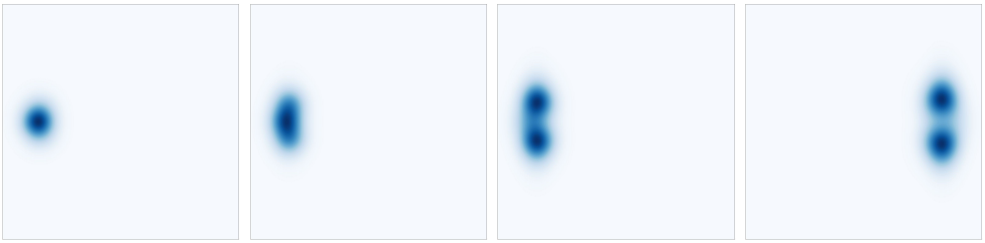

$(n = 29)$ $t = 9 \cdot 10^{-3}$ $t = 3.98 \cdot 10^{-2}$ $t = 7.11 \cdot 10^{-2}$ $t = 8.59 \cdot 10^{-2}$

Figure 17. Snapshots of the density profile $|u(\mathbf{x}, t)|^2$ at various times during the harmonically trapped re-collisions between the two components of a binary condensate. Top row: experiment $n = 28$ of Table 5 ($\gamma_1 = \gamma_2 = 1$, $\gamma_{12} = -200$, $c_1 = c_2$) and snapshots relative to the first consecutive collisions, at the instants of velocity inversion. Bottom row: experiment $n = 29$ ($\gamma_1 = \gamma_2 = -1$, $\gamma_{12} = 50$, $c_1 = c_2$) and snapshots relative to the first, third, fifth and sixth collision. For visualization purposes, along each row the snapshots have a different scale: the absolute scale can be inferred from Figure 18.

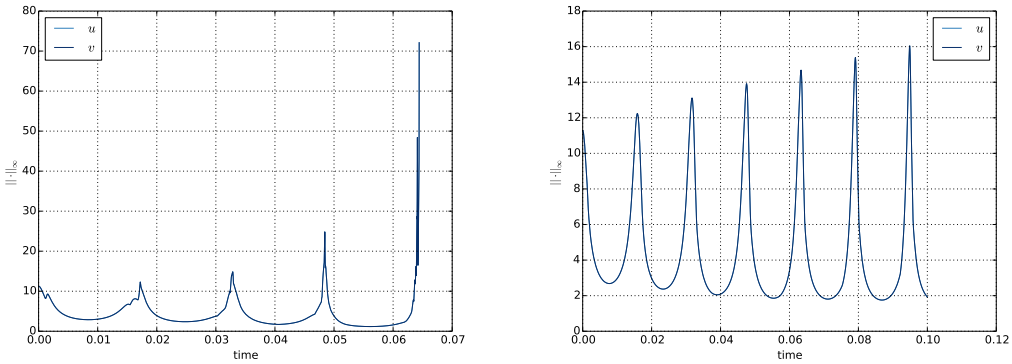

$(n = 28)$ $\gamma_1 = \gamma_2 = 1$, $\gamma_{12} = -200$ $(n = 29)$ $\gamma_1 = \gamma_2 = -1$, $\gamma_{12} = 50$

Figure 18. Time behaviour of the norm $\|u(\cdot, t)\|_\infty$ during the harmonically trapped multiple re-collision process between the two components of a binary condensate, relative to experiments $n = 28$ (left) and $n = 29$) (right) of Table 5. Since the two populations are the same, by symmetry $\|v(\cdot, t)\|_\infty = \|u(\cdot, t)\|_\infty$.

hits for the first time the much lighter one, the former drags the latter in an almost periodic motion within the trap. The rapid mass concentration occurring at each collision results in a corresponding jump of the L^∞-norms of the solutions. These phenomena are

visualised in Figure 15 for the experiments $n = 24, 25, 27$ of Table 5.

Pushing further the unbalance in the population ratios, what we had found in the single collision case (last row of Figure 4) was the complete destruction of the localisation of the light component and its spread in almost all radial directions, with a larger part of its mass scattered in the direction of the incident heavy component. The confining potential has now the effect of focusing the outgoing annular wave of the light component profile back to the centre of the trap, where the cycle is then repeated. After multiple re-collisions the annular wave of the light component deteriorates in several fringes. This phenomenon is visualised in Figure 16 for the experiments $n = 26$ of Table 5.

Turning to the analysis of the effects of competing interactions on the multiple re-collisions of two equally populated components, two most relevant cases are the 'squeezing-and-shooting' scattering realised when the inter-species attraction has a much stronger magnitude than the intra-species repulsion (case $n = 28$ of Table 5), and the 'splash' effect realised when the inter-species repulsion has a much stronger magnitude than the intra-species repulsion ($n = 29$). We investigate both of them in Figures 17 and 18. In the former case in each cycle the phenomenon is qualitatively replicated, with more and more mass concentration arising in the course of the subsequent collisions, until when a proper blow-up occurs in the density profile of each component (its L^∞-norm diverges in finite time). In the latter case too the phenomenon is repeated almost periodically, thanks to the re-focusing effect of the trap, and at each new collision a new 'splash' takes place of one component against the other: the L^∞-norm of each components reaches its local maximum at the instants of largest spatial overlap at the centre of the trap, and its local minimum at the instants of velocity inversion, with such minima decreasing slightly at each cycle due to the mild focusing effect of the intra-component attraction.

Acknowledgments

This work was partially supported by the 2014-2017 MIUR-FIR grant "*Cond-Math: Condensed Matter and Mathematical Physics*", code RBFR13WAET.

References

[1] M. H. Anderson, J. R. Ensher, M. R. Matthews, C. E. Wieman, and E. A. Cornell, *Observation of Bose-Einstein Condensation in a Dilute Atomic Vapor*, Science, 269 (1995), pp. 198–201.

[2] W. Bao, *Ground States and Dynamics of Multicomponent Bose–Einstein Condensates*, Multiscale Modeling & Simulation, 2 (2004), pp. 210–236.

[3] W. Bao and Y. Cai, *Mathematical theory and numerical methods for Bose-Einstein condensation*, Kinetic and Related Models, 6 (2013), pp. 1–135.

[4] W. Bao, Q. Du, and Y. Zhang, *Dynamics of Rotating Bose–Einstein Condensates and its Efficient and Accurate Numerical Computation*, SIAM Journal on Applied Mathematics, 66 (2006), pp. 758–786.

[5] W. Bao and D. Jaksch, *An Explicit Unconditionally Stable Numerical Method for Solving Damped Nonlinear Schrödinger Equations with a Focusing Nonlinearity*, SIAM Journal on Numerical Analysis, 41 (2003), pp. 1406–1426.

[6] W. Bao, D. Jaksch, and P. A. Markowich, *Numerical solution of the Gross–Pitaevskii equation for Bose–Einstein condensation*, Journal of Computational Physics, 187 (2003), pp. 318–342.

[7] W. Bao and J. Shen, *A Fourth-Order Time-Splitting Laguerre–Hermite Pseudospectral Method for Bose–Einstein Condensates*, SIAM Journal on Scientific Computing, 26 (2005), pp. 2010–2028.

[8] N. Benedikter, M. Porta, and B. Schlein, *Effective evolution equations from quantum dynamics*, vol. 7 of Springer Briefs in Mathematical Physics, Springer, Cham, 2016.

[9] H. Berland, B. Owren, and B. Skaflestad, *Solving the nonlinear Schrödinger equation using exponential integrators*, Modeling, Identification and Control, 27 (2006), pp. 201–217.

[10] C. Canuto, M. Y. Hussaini, A. Quarteroni, and T. Zhang, *Spectral Methods*, vol. 1, Springer, 2006.

[11] T. Cazenave, *Semilinear Schrödinger equations*, vol. 10 of Courant Lecture Notes in Mathematics, New York University Courant Institute of Mathematical Sciences, New York, 2003.

[12] M. Cerimele, F. Pistella, and S. Succi, *Particle-inspired scheme for the Gross–Pitaevski equation: An application to Bose–Einstein condensation*, Computer Physics Communications, 129 (2000), pp. 82–90.

[13] M. M. Cerimele, M. L. Chiofalo, F. Pistella, S. Succi, and M. P. Tosi, *Numerical solution of the Gross-Pitaevskii equation using an explicit finite-difference scheme: An application to trapped Bose-Einstein condensates*, Phys. Rev. E, 62 (2000), pp. 1382–1389.

[14] J. Chen and B. Guo, *Blow-up profile to the solutions of two-coupled Schrödinger equations*, Journal of Mathematical Physics, 50 (2009).

[15] S. T. Chui, V. N. Ryzhov, and E. E. Tareyeva, *Phase separation and vortex states in binary mixture of Bose-Einstein condensates in trapping potentials with displaced centers*, Journal of Experimental and Theoretical Physics Letters, 75 (2002), pp. 233–237.

[16] K. B. Davis, M. O. Mewes, M. R. Andrews, N. J. van Druten, D. S. Durfee, D. M. Kurn, and W. Ketterle, *Bose-Einstein Condensation in a Gas of Sodium Atoms*, Phys. Rev. Lett., 75 (1995), pp. 3969–3973.

[17] F. J. Dyson, E. H. Lieb, and B. Simon, *Phase transitions in quantum spin systems with isotropic and nonisotropic interactions*, Journal of Statistical Physics, 18 (1978), pp. 335–383.

[18] L. Fanelli and E. Montefusco, *On the blow-up threshold for weakly coupled nonlinear Schrödinger equations*, J. Phys. A, 40 (2007), pp. 14139–14150.

[19] D. S. Hall, *Multi-Component Condensates: Experiment*, Springer Berlin Heidelberg, Berlin, Heidelberg, 2008, pp. 307–327.

[20] D. S. Hall, M. M. E., J. R. Enscher, C. E. Wieman, and E. A. Cornell, *The Dynamics of Component Separation in a Binary Mixture of Bose-Einstein Condensates*, Phys. Rev. Lett., 81 (1998), pp. 1539–1542.

[21] M. Jeblick, N. Leopold, and P. Pickl, *Derivation of the Time Dependent Gross-Pitaevskii Equation in Two Dimensions*, arXiv.org:1608.05326 (2016).

[22] A. Jüngel and R.-M. Weishäupl, *Blow-up in two-component nonlinear Schrödinger systems with an external driven field*, Mathematical Models and Methods in Applied Sciences, 23 (2013), pp. 1699–1727.

[23] T. Kennedy, E. H. Lieb, and B. S. Shastry, *The* XY *Model Has Long-Range Order for All Spins and All Dimensions Greater than One*, Phys. Rev. Lett., 61 (1988), pp. 2582–2584.

[24] K. Kirkpatrick, B. Schlein, and G. Staffilani, *Derivation of the two dimensional nonlinear Schrödinger equation from many body quantum dynamics*, American Journal of Mathematics, 133 (2011), pp. 91–13.

[25] A. Knowles and P. Pickl, *Mean-field dynamics: singular potentials and rate of convergence*, Comm. Math. Phys., 298 (2010), pp. 101–138.

[26] L. Kong, J. Hong, and J. Zhang, *LOD-MS for Gross-Pitaevskii Equation in Bose-Einstein Condensates*, Communications in Computational Physics, 14 (2015), pp. 219–241.

[27] K. L. Lee, N. B. Jørgensen, I.-K. Liu, L. Wacker, J. J. Arlt, and N. P. Proukakis, *Phase separation and dynamics of two-component bose-einstein condensates*, Phys. Rev. A, 94

(2016).

[28] A. J. Leggett, *Bose-Einstein condensation in the alkali gases: some fundamental concepts*, Rev. Mod. Phys., 73 (2001), pp. 307–356.

[29] X. Li, Y. Wu, and S. Lai, *A sharp threshold of blow-up for coupled nonlinear Schrödinger equations*, Journal of Physics A: Mathematical and Theoretical, 43 (2010), p. 165205.

[30] E. H. Lieb, R. Seiringer, J. P. Solovej, and J. Yngvason, *The mathematics of the Bose gas and its condensation*, vol. 34 of Oberwolfach Seminars, Birkhäuser Verlag, Basel, 2005.

[31] T.-C. Lin and J. Wei, *Solitary and self-similar solutions of two-component system of nonlinear Schrödinger equations*, Physica D: Nonlinear Phenomena, 220 (2006), pp. 99–115.

[32] L. Ma and L. Zhao, *Sharp thresholds of blow-up and global existence for the coupled nonlinear Schrödinger system*, Journal of Mathematical Physics, 49 (2008).

[33] B. Malomed, *Multi-Component Bose-Einstein Condensates: Theory*, Springer Berlin Heidelberg, Berlin, Heidelberg, 2008, pp. 287–305.

[34] M. W. Mancini, G. D. Telles, A. R. L. Caires, V. S. Bagnato, and L. G. Marcassa, *Observation of Ultracold Ground-State Heteronuclear Molecules*, Phys. Rev. Lett., 92 (2004), p. 133203.

[35] A. Michelangeli, *Role of scaling limits in the rigorous analysis of Bose-Einstein condensation*, J. Math. Phys., 48 (2007), p. 102102.

[36] ——, *Equivalent definitions of asymptotic 100% BEC*, Nuovo Cimento Sec. B., (2008), pp. 181–192.

[37] A. Michelangeli and A. Olgiati, *Mean-field quantum dynamics for a mixture of Bose–Einstein condensates*, Analysis and Mathematical Physics, 7 (2017), pp. 377–416.

[38] J. Ming, Q. Tang, and Y. Zhang, *An efficient spectral method for computing dynamics of rotating two-component Bose–Einstein condensates via coordinate transformation*, Journal of Computational Physics, 258 (2014), pp. 538–554.

[39] G. Modugno, G. Ferrari, G. Roati, R. J. Brecha, A. Simoni, and M. Inguscio, *Bose-Einstein Condensation of Potassium Atoms by Sympathetic Cooling*, Science, 294 (2001), pp. 1320–1322.

[40] G. Modugno, M. Modugno, F. Riboli, G. Roati, and M. Inguscio, *Two Atomic Species Superfluid*, Phys. Rev. Lett., 89 (2002), p. 190404.

[41] E. J. Mueller, T.-L. Ho, M. Ueda, and G. Baym, *Fragmentation of Bose-Einstein condensates*, Phys. Rev. A, 74 (2006), p. 033612.

[42] C. J. Myatt, E. A. Burt, R. W. Ghrist, E. A. Cornell, and C. E. Wieman, *Production of Two-overlapping Bose-Einstein Condensates by Sympathetic Cooling*, Phys. Rev. Lett., 78 (1997), pp. 586–589.

[43] P. T. Nam, N. Rougerie, and R. Seiringer, *Ground states of large bosonic systems: the Gross–Pitaevskii limit revisited*, Anal. PDE, 9 (2016), pp. 459–485.

[44] A. Olgiati, *Effective Non-linear Dynamics of Binary Condensates and Open Problems*, in Advances in Quantum Mechanics: Contemporary Trends and Open Problems, G. Dell'Antonio and A. Michelangeli, eds., Springer INdAM Series, Springer International Publishing, 2017, pp. 239–256.

[45] S. B. Papp and C. E. Wieman, *Observation of Heteronuclear Feshbach Molecules from a* ^{85}Rb$^{\smile}$^{87}Rb *Gas*, Phys. Rev. Lett., 97 (2006), p. 180404.

[46] O. Penrose and L. Onsager, *Bose-Einstein Condensation and Liquid Helium*, Phys. Rev., 104 (1956), pp. 576–584.

[47] P. Pickl, *Derivation of the time dependent Gross-Pitaevskii equation without positivity condition on the interaction*, J. Stat. Phys., 140 (2010), pp. 76–89.

[48] ——, *A simple derivation of mean field limits for quantum systems*, Lett. Math. Phys., 97 (2011), pp. 151–164.

[49] ——, *Derivation of the time dependent Gross-Pitaevskii equation with external fields*, Rev. Math. Phys., 27 (2015), pp. 1550003, 45.

[50] L. Pitaevskii and S. Stringari, *Bose-Einstein Condensation and Superfluidity*, Oxford

University Press, 2016.

[51] P. A. Ruprecht, M. J. Holland, K. Burnett, and M. Edwards, *Time-dependent solution of the nonlinear Schrödinger equation for Bose-condensed trapped neutral atoms*, Phys. Rev. A, 51 (1995), pp. 4704–4711.

[52] H. Salman, *A time-splitting pseudospectral method for the solution of the Gross–Pitaevskii equations using spherical harmonics with generalised-Laguerre basis functions*, Journal of Computational Physics, 258 (2014), pp. 185–207.

[53] B. Schlein, *Dynamics of Bose-Einstein Condensates*, arXiv.org:0704.0813 (2007).

[54] ——, *Derivation of Effective Evolution Equations from Microscopic Quantum Dynamics*, arXiv.org:0807.4307 (2008).

[55] A. White, T. Hennessy, and T. Busch, *Emergence of classical rotation in superfluid Bose-Einstein condensates*, Phys. Rev. A, 93 (2016), p. 033601.

[56] Q.-b. Xu and Q.-s. Chang, *New numerical methods for the coupled nonlinear Schrödinger equations*, Acta Mathematicae Applicatae Sinica, English Series, 26 (2010), pp. 205–218.

[57] Y. Zhang, W. Bao, and H. Li, *Dynamics of rotating two-component Bose–Einstein condensates and its efficient computation*, Physica D: Nonlinear Phenomena, 234 (2007), pp. 49–69.